

10-2013

## Investigation of Grid Adaptation to Reduce Computational Efforts for a 2-D Hydrogen-Fueled Dual-Mode Scramjet

Kam Keong Foo  
*Embry-Riddle Aeronautical University - Daytona Beach*

Follow this and additional works at: <https://commons.erau.edu/edt>



Part of the [Aerodynamics and Fluid Mechanics Commons](#)

---

### Scholarly Commons Citation

Foo, Kam Keong, "Investigation of Grid Adaptation to Reduce Computational Efforts for a 2-D Hydrogen-Fueled Dual-Mode Scramjet" (2013). *Dissertations and Theses*. 67.  
<https://commons.erau.edu/edt/67>

This Thesis - Open Access is brought to you for free and open access by Scholarly Commons. It has been accepted for inclusion in Dissertations and Theses by an authorized administrator of Scholarly Commons. For more information, please contact [commons@erau.edu](mailto:commons@erau.edu).

**Investigation of Grid Adaptation to Reduce Computational Efforts  
for a 2-D Hydrogen-Fueled Dual-Mode Scramjet**

by

Kam Keong Foo

A Thesis Submitted to the  
Graduate Studies Office  
in Partial Fulfillment of the Requirements for the Degree of  
Master of Science in Aerospace Engineering

Embry-Riddle Aeronautical University

Daytona Beach, Florida

October 2013

**Investigation of Grid Adaptation to Reduce Computational Efforts  
for a 2-D Hydrogen-Fueled Dual-Mode Scramjet**

by

Kam Keong Foo

This thesis was prepared under the direction of the candidate's thesis committee chairman, Dr. William A. Engblom, Department of Mechanical Engineering, and has been approved by the members of his thesis committee. It was submitted to the Aerospace Engineering Department and was accepted in partial fulfillment of the requirements for the degree of Master of Science in Aerospace Engineering.

Thesis Committee:



Dr. William A. Engblom

Chairman



Dr. Reda R. Mankbadi

Member



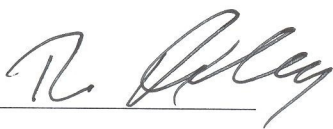
Dr. Eric Perrell

Member

*on behalf A. Lyubovits*

Dr. Yi Zhao

Graduate Program Coordinator



Dr. Robert Oxley

10-23-13

Associate Vice President for Academics

## **Acknowledgments**

I would like to express my gratitude and appreciation to my advisor, Dr. William A. Engblom, for his technical expertise, constructive suggestions, and encouragement throughout and beyond the undertaking of this study. The completion of this research work would not be possible without his guidance and support. I would also like to thank Dr. Reda R. Mankbadi and Dr. Eric Perrell for taking the time and effort to serve on my thesis committee. Special thanks to Dr. Sandra Boetcher for her help on using the Zeus cluster. I would also like to thank Dr. David J. Sypeck for giving me the opportunity to teach and learn as a graduate teaching assistant.

My sincere gratitude extends to Prathikshen Selvadorai, Michael Borghi, Domenic Barsotti and all my friends and colleagues for their technical help and simply being my friends.

With all my heart, I would like to thank my parents, Paul and Mary, and my brother and sister for their unconditional support both financially and emotionally throughout my graduate studies. Last but not least, I would like to thank my girlfriend, Teck Hong, for always being there to support me through good times and bad.

## Abstract

Author: Kam Keong Foo  
Title: Investigation of Grid Adaptation to Reduce Computational Efforts for a  
2-D Hydrogen-Fueled Dual-Mode Scramjet  
Institution: Embry-Riddle Aeronautical University  
Degree: Master of Science in Aerospace Engineering  
Year: 2013

A two-dimensional dual-mode scramjet flowpath is developed and evaluated using the ANSYS Fluent density-based flow solver with various computational grids. Results are obtained for fuel-off, fuel-on non-reacting, and fuel-on reacting cases at different equivalence ratios. A one-step global chemical kinetics hydrogen-air model is used in conjunction with the eddy-dissipation model. Coarse, medium and fine computational grids are used to evaluate grid sensitivity and to investigate a lack of grid independence. Different grid adaptation strategies are performed on the coarse grid in an attempt to emulate the solutions obtained from the finer grids. The goal of this study is to investigate the feasibility of using various mesh adaptation criteria to significantly decrease computational efforts for high-speed reacting flows.

## Table of Content

I. Introduction	1
II. Background	4
III. Methodology	6
A. Computational Mesh	6
B. Physical Models and Boundary Conditions	7
C. Procedure	10
IV. Results	12
A. $\Phi = 0.00$ (Fuel-Off)	12
B. $\Phi = 0.27$	15
C. $\Phi = 0.38$	21
D. $\Phi = 0.38$ (Transient)	26
V. Grid Adaptation Sensitivity Study	32
VI. Summary and Conclusions	42
References	44

## List of Figures

Figure 1	2
Figure 2	2
Figure 3	5
Figure 4	5
Figure 5	6
Figure 6	7
Figure 7	11
Figure 8	13
Figure 9	14
Figure 10	14
Figure 11	15
Figure 12	17
Figure 13	18
Figure 14	19
Figure 15	20
Figure 16	21
Figure 17	22

Figure 18	23
Figure 19	24
Figure 20	25
Figure 21	26
Figure 22	29
Figure 23	30
Figure 24	31
Figure 25	34
Figure 26	35
Figure 27	38
Figure 28	39
Figure 29	40
Figure 30	41



## List of Tables

Table 1	10
Table 2	36

## List of Equations

Equation 1	8
Equation 2	8
Equation 3	8
Equation 4	8
Equation 5	8
Equation 6	9
Equation 7	9
Equation 8	9
Equation 9	9
Equation 10	9
Equation 11	11

## Nomenclature

$A, B$	= Magnussen constant for reactants (default 4.0) and products (default 0.5)
$A_r$	= pre-exponential factor
$\beta_r$	= temperature exponent
$C_{j,r}$	= molar concentration of species $j$ in reaction $r$
$\eta'_{j,r}$	= rate exponent for reactant species $j$ in reaction $r$
$\varepsilon$	= turbulent dissipation rate
$E_r$	= activation energy
$\gamma_{j,r}$	= third body efficiency of species $j$ in reaction $r$
$\Gamma$	= net effect of third bodies on reaction rate
$J$	= diffusion flux of species $i$
$k$	= turbulent kinetic energy
$k_{global}$	= global one-step rate constant
$k_{f,r}, k_{b,r}$	= forward and backward rate constant for reaction $r$
$M_{w,i}$	= molecular weight of species $i$
$N$	= number of chemical species in the system
$\Phi$	= fuel equivalence ratio
$\rho$	= density
$R$	= universal gas constant
$R_i$	= net reaction rate
$\hat{R}_{i,r}$	= Arrhenius molar rate of creation/destruction of species $i$ in reaction $r$
$S_i$	= rate of creation by addition from dispersed phase plus any user-defined sources
$\tau$	= large-eddy mixing time scale

$T$	= temperature
$v$	= velocity
$v'_{i,r}$	= stoichiometric coefficient of reactant $i$ in reaction $r$
$v''_{i,r}$	= stoichiometric coefficient of product $i$ in reaction $r$
$v''_{j,r}$	= stoichiometric coefficient for product $j$ in reaction $r$
$Y_i$	= mass fraction of species $i$
$Y_R$	= mass fraction of particular reactant $R$
$Y_P$	= mass fraction of any product species $P$

## I. Introduction

As hypersonic and scramjet research have advanced significantly in the recent decades, sophisticated and cost effective numerical tools are essential in supporting ground-based wind tunnel testing. However, high fidelity numerical simulations of these turbulent and chemically-reacting flowfields require enormous and costly computational resources. One way of reducing computational efforts is to utilize computational grids efficiently and at locations where necessary. This study focuses on employing grid adaptation as a tool to refine solutions obtained using low density grids.

Generally speaking, there are two types of grid adaptation methods; grid point redistribution and grid point addition. In the former method, the number of grid points in the domain remains the same. In the adaption process, grid points are redistributed to areas of interest based on the flow solution. However, doing so deprives the other flow regions of adequate resolution and could also cause excessive grid skewing and stretching [1]. A numerical study on hypersonic nozzle flow was done by Hsu [2] using this adaptation method and reasonable results were obtained. Singh and Ramakrishnan [3] performed a numerical modeling of scramjet combustor flowfields using this adaptation method and found that the adaptation did enhance the original grid solution. Figure 1 shows the grid point redistribution method used by Singh et al. in their study. The grid points were redistributed to better capture the shock upstream of the injector plume and cells that are stretched and skewed can be observed. The second adaptation method involves adding additional grid points to the original grid but at the expense of increase in required computational resources. However, it does not have the drawbacks of the former method. Numerical simulations of hypersonic air intake flow were done by Frauholz et al [4] using a mesh-adaptive approach (with grid point addition method) and obtained superior

results. Figure 2 shows the grid point addition method used in the work done by Frauholz et al. Additional grid points were added to the original grid to better resolve the shocks created by the hypersonic air intake. As a result, more cells were created and a more accurate solution was achieved. All in all, adaptive refinement aims to reduce the global truncation errors of a relatively coarser grid solution without globally refining the entire grid. In the current study, the second adaptation method will be used.

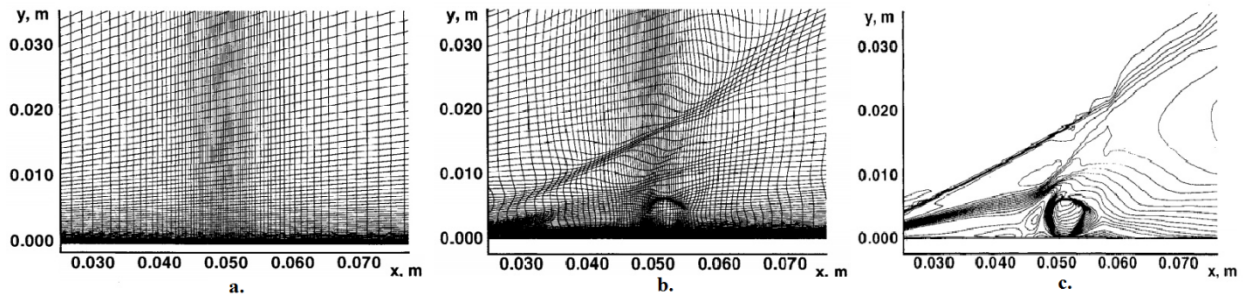


**Figure 1, Grid Point Redistribution Method for a Combustor with fuel injector at  $X = 0.05$  m: a) Unadapted Grid, b) Adapted Grid, c) Mach Number Contours [3]**

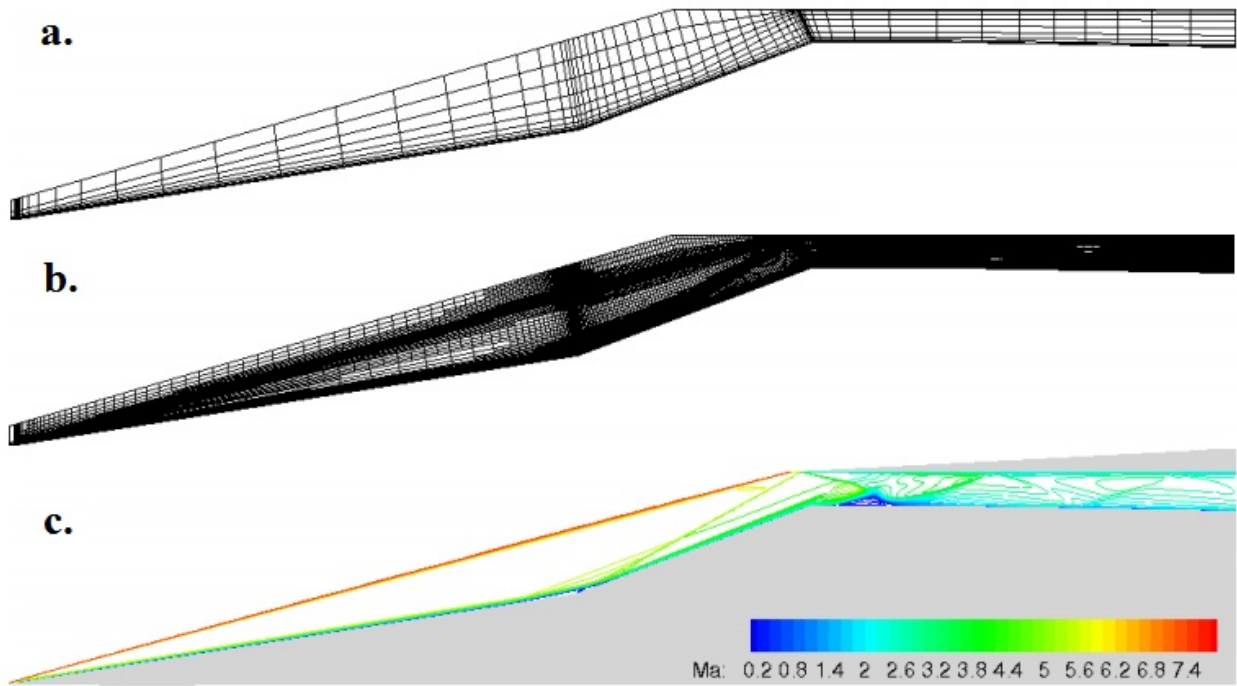


**Figure 2, Grid Point Addition Method for a Hypersonic Air Intake, a) Unadapted Grid, b) Adapted Grid, c) Mach Number Contours [4]**

The Supersonic Combustion Facility's (SCF) flowpath at University of Virginia (UVa.) was chosen for this research as results from previous studies have shown that numerical simulations were successful in replicating the experimental data to a reasonable level of accuracy [5,6,7]. However, grid independent solutions were not obtained, and are especially difficult to obtain for high-speed propulsion flows due to the level of computational effort required. The goal of this research is to explore how well different grid adaptation schemes lower computational costs in pursuit of grid independent solutions.

## II. Background

The SCF at UVa. is a vertically mounted direct-connect dual-mode scramjet flowpath. Figure 3 shows the schematic of the facility and the supply nozzle, isolator, combustor, extender, fuel lines, coolant lines and numerous pressure transducers and thermocouples [6]. Figure 4 shows the basic dimension of the flowpath. The facility is an electrically heated, clean-air, supersonic flowpath which is capable of simulating flight Mach numbers near 5 and has continuous flow capability to allow unlimited duration scramjet testing [8]. A 300 kW, 14 stage electrical heater provides vitiated free airflow of about 1200 K to the supply nozzle. The facility also has the capability to add make-up oxygen, as well as controlled amounts of H<sub>2</sub>O and CO<sub>2</sub> vitiates to simulate larger tunnels heated by hydrogen or hydrocarbon.

Mach 2 flow is delivered to the isolator by the convergent-divergent supply nozzle. The isolator and combustor have a constant cross-sectional area of 1.5 x 1.0 square inch. At the end of the isolator is a compression ramp which houses a conical fuel-injector that delivers a Mach 1.7 jet stream of hydrogen fuel. The compression ramp angle is 10° and has a base height of 0.25 inch. Aft of the combustor is a 2.9° extender-nozzle. The airflow exhausts to the ambient atmosphere and the exhaust plume is captured by a catch-cone and directed out of the facility.

This facility is not capable of auto-ignition. When the hydrogen fuel is injected into the core flow and reaches a steady-state, a detonation-driven ignition system is used to ignite the fuel. Combustion is self-sustaining once the engine is ignited.



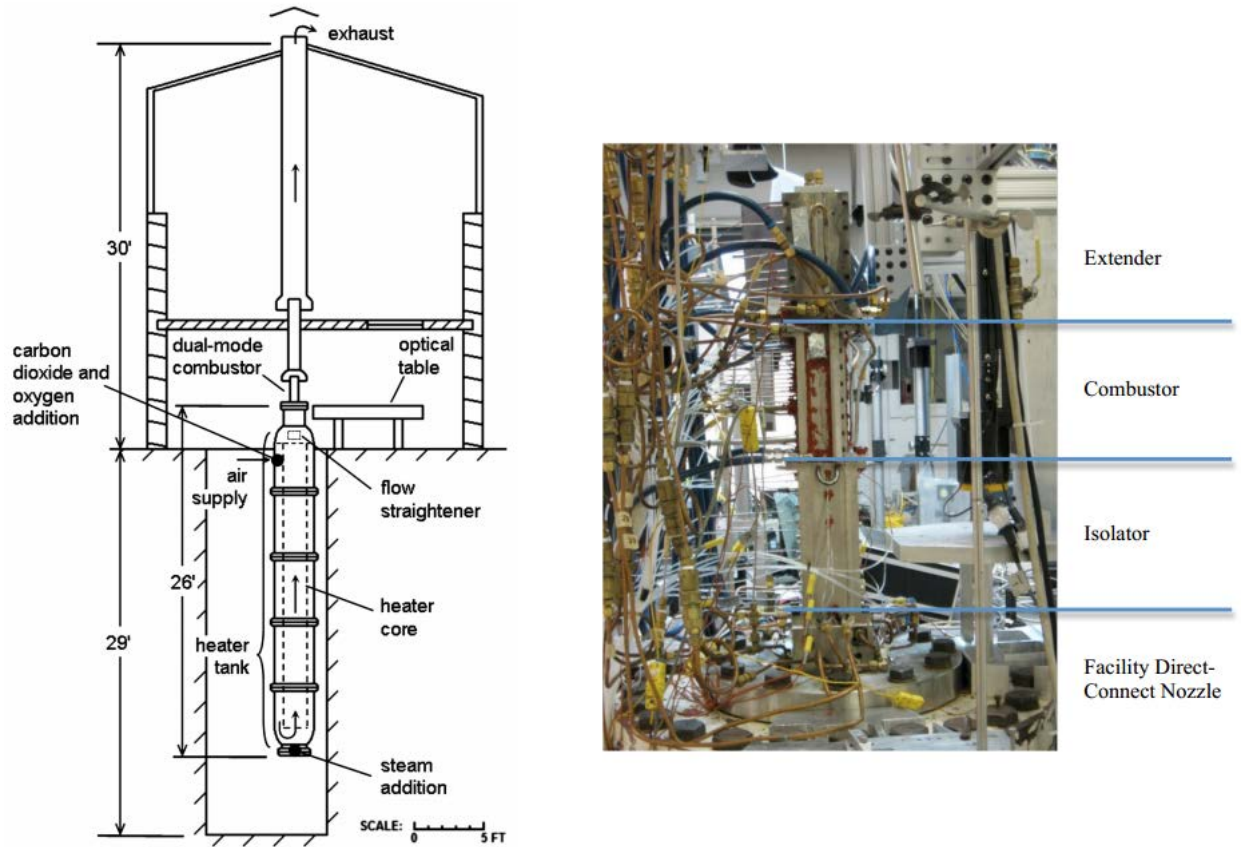


Figure 3, UVa. SCF Schematic [8], Supersonic Combustion Facility [6]

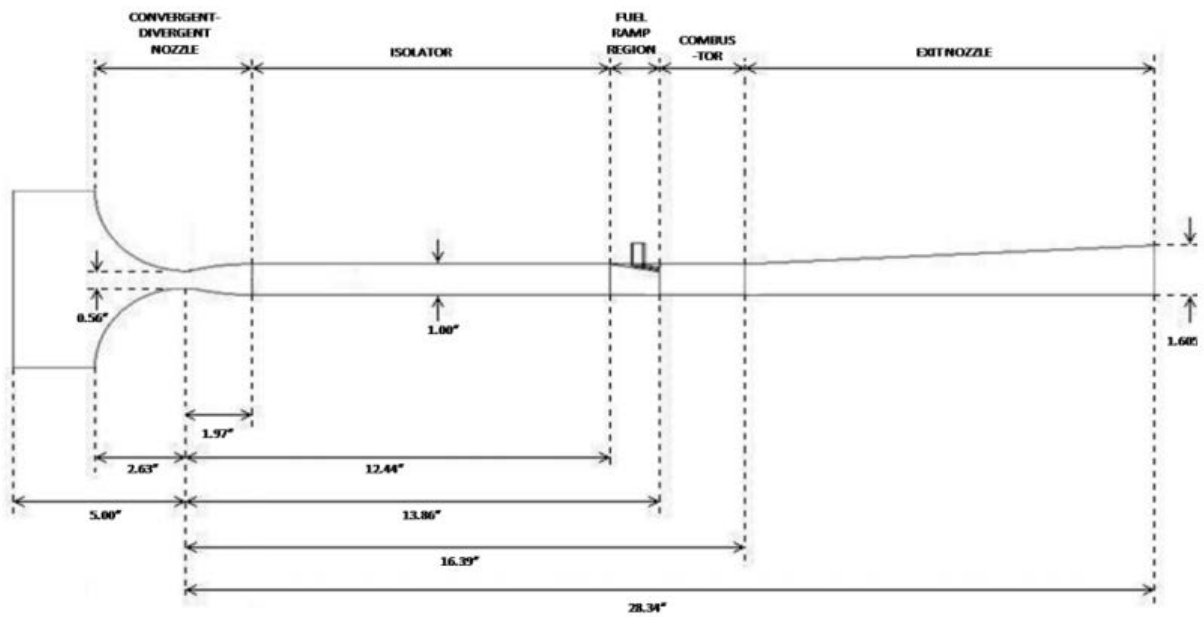
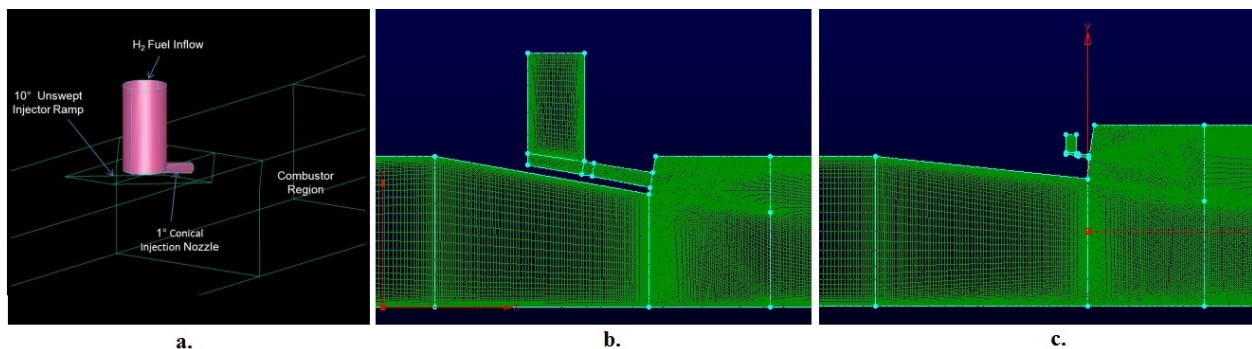


Figure 4, UVa. Dual-Mode Scramjet Flowpath Schematic and Basic Dimensions [5]

### III. Methodology

#### A. Computational Mesh

The flowpath of UVa's SCF was adapted and simplified for this research. The compression ramp angle upstream of the combustor was decreased from 10 degrees to 6 degrees to increase the cross-sectional area of the combustor inlet; to minimize potential for unstart of the combustor, similar to the approach taken in Flowpath B [7]. In the three-dimensional version of the SCF, the flow remains in scram mode at modest equivalence ratios in part because the 10 degree compression ramp does not span the entire width of the flowpath. The width of the injector geometry was also reduced to allow similar fuel-air equivalence ratios as intended for the original UVa. SCF. If the original diameter was retained as the width, the total pressure of the hydrogen fuel plenum would have to be lowered drastically in order to achieve appropriate mass flow rates. The fuel jet would then be over-expanded, causing adverse effects in fuel penetration and mixing in the combustor. The combustor and extender nozzle sections were given a 20 percent increase in height by raising the top walls to allow better pressure relieve during combustion and avoid unstart. Figure 5 shows the modifications from 3-dimensional to 2-dimensional model.



**Figure 5, a) 3-Dimensional compression ramp [5], b) 3-Dimensional model plane view, c) 2-Dimensional model plane view**

Three computational grids consisting of structured blocks were developed and examined in the course of the simulations with ANSYS Fluent; a coarse grid consisting of ~26,000 cells, a medium grid consisting of ~107,000 cells, and a fine grid consisting of ~427,000 cells. Figure 6 shows the coarse grid with colored planes denoting different sections of the flowpath. Higher grid resolution was applied to areas of interest such as the isolator, compression ramp, combustor, and fuel injector to resolve key flow features. Grid-to-wall strategy was used along the entire flowpath to better capture the shock boundary layer interactions and boundary layer separations. As a result,  $y^+$  values of less than 5 were achieved for first cell off walls.

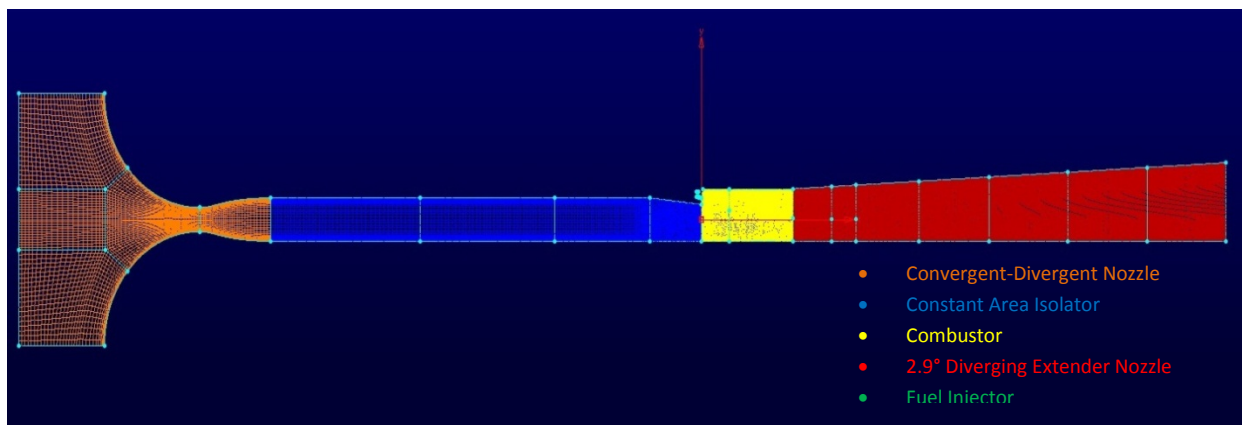


**Figure 6, 2-Dimensional Structured Mesh**

## **B. Physical Models and Boundary Conditions**

The commercial CFD solver ANSYS Fluent has been used to perform the numerical simulations for this research work. Steady-state Reynolds-Averaged Navier-Stokes (RANS) solutions are obtained. The density-based solver with second-order upwind discretization using AUSM flux-difference splitting scheme was chosen. The realizable  $k$ - $\epsilon$  turbulence model with enhanced wall treatment (i.e., grid-to-the-wall strategy) and pressure gradient effects was used with a turbulent Schmidt number of 0.6, based on the success of previous research [6]. The realizable  $k$ - $\epsilon$  turbulence model accurately predicts the spreading rate of both planar and round

jets, and is also likely to provide superior performance for flows involving rotation, boundary layers under strong adverse pressure gradients, separation, and recirculation [10]. Species volumetric reactions were employed using the combination of laminar finite-rate and eddy-dissipation models.

The laminar finite-rate model does not take into account the effects of turbulence fluctuations. The source terms in the species transport equation, Eqn 1, are computed as the sum of the reaction rates, Eqn 2. For a reversible reaction, the molar rate of creation/destruction of species  $i$  in reaction  $r$  is given by Eqn 3. The forward rate constant for reaction  $r$ ,  $k_{f,r}$ , is calculated using the Arrhenius kinetic expression, Eqn 5.

$$\frac{\partial}{\partial t}(\rho Y_i) + \nabla \cdot (\rho \vec{v}) Y_i = -\nabla \cdot \vec{J}_i + R_i + S_i \quad (1)$$

$$R_i = M_{w,i} \sum_{r=1}^{N_R} \hat{R}_{i,r} \quad (2)$$

$$\hat{R}_{i,r} = \Gamma(v''_{i,r} - v'_{i,r}) \left( k_{f,r} \prod_{j=1}^N [C_{j,r}]^{\eta'_{j,r}} - k_{b,r} \prod_{j=1}^N [C_{j,r}]^{v''_{j,r}} \right) \quad (3)$$

$\Gamma$  represents the net effect of third bodies on the reaction rate and can be expressed as Eqn 4.

$$\Gamma = \sum_j^N \gamma_{j,r} C_j \quad (4)$$

$$k_{f,r} = A_r T^{\beta_r} e^{-\frac{E_r}{RT}} \quad (5)$$

The eddy-dissipation model in ANSYS Fluent is a turbulence-chemistry model based on the work of Magnussen and Hjertager [11]. This model is based on the assumption that chemical reactions occur much faster than turbulence mixing. For fast burning fuels, the overall reaction rate depends on the turbulent mixing rate and chemical kinetic rate is neglected. The local turbulent mixing rate is related to the local time scale or frequency of the turbulence present in

the flow. This time scale is expressed as  $\tau$ , Eqn 6, and is related to the turbulent kinetic energy and turbulent dissipation rate.

$$\tau = \frac{k}{\varepsilon} \quad (6)$$

The reaction rate is estimated from the mass fractions of reactants and products, and depends on the turbulent mixing time scale; Eqn 7 and Eqn 8. The smaller of the two expressions is used as the reaction rate is limited by the deficient mean species, which may be combustion products to take into account the existence of burnt gases, providing the energy required to ignite fresh reactants [12].

$$R_{i,r} = v'_{i,r} M_{w,i} A \rho \frac{\varepsilon}{k} \min \left( \frac{Y_R}{v'_{R,r} M_{w,R}} \right) \quad (7)$$

$$R_{i,r} = v'_{i,r} M_{w,i} A B \rho \frac{\varepsilon \sum_P Y_P}{k \sum_j^N v''_{j,r} M_{w,j}} \quad (8)$$

The finite-rate/eddy-dissipation model, which is a combination of the two aforementioned reaction models, is available in Ansys Fluent and is utilized in this study. In this model, the chemical kinetic rates, Eqn 2, and eddy-dissipation rates, Eqn 4 and Eqn 5, are determined and the smaller of the two models will be used. The Marinov-Westbrook global one-step reaction chemical kinetics model for hydrogen-air was implemented for combustion modeling [13]. The one-step reaction and rate constant expression in Arrhenius form are shown in Eqn 9 and Eqn 10, respectively.



$$k_{global} = 5.692 \times 10^{11} e^{-\frac{1.464 \times 10^8}{RT}} [H_2]^{1.0} [O_2]^{0.5} \quad (10)$$

Isothermal wall temperature of 1000 K was chosen for the combustor section and 500 K for the supply nozzle, isolator, and extender nozzle. Respective boundary conditions for different equivalence ratios are listed in Table 1. Ambient condition is applied at the outlet of the extender-nozzle. These run conditions are similar to those used to evaluate the original UVa. SCF in [6].

**Table 1, Boundary Conditions**

Simulation Number	Equivalence Ratio, $\phi$	Stagnation Condition		Ambient Condition
		Supply Nozzle	H2 Fuel Plenum	
#1	0.00	$P_o = 327.12 \text{ kPa}$ $T_o = 1202 \text{ K}$	---	$P_{\text{atm}} = 99.1 \text{ kPa}$ $T_{\text{atm}} = 294.4 \text{ K}$
#2	0.27		$P_o = 200 \text{ kPa}$	
#3	0.38		$P_o = 300 \text{ kPa}$	

### C. Procedure

A non-reacting solution is obtained first for the initial (#1) run condition and used to initialize the other two simulations. When the laminar finite-rate volumetric reaction is turned on, the activation energy of the global one-step reaction is decreased by a factor of 2 and run for several thousand iterations to numerically ‘ignite’ the fuel. This is necessary as the temperature of the flow in the combustor is not sufficient for auto-ignition. Once substantial pressurization is achieved, the activation energy is returned to its standard value. When convergence is obtained, the eddy-dissipation model is activated and run until final convergence is achieved. Convergence was determined based on monitoring the 1) residuals of Reynolds-Averaged Navier-Stokes equations, and more importantly, 2) water vapor mass flux at exit plane. Similar procedures were applied to the coarse, medium and fine grids. Global adaptation was performed on the coarse grid to generate the medium and fine grids, sequentially. Figure 7 illustrates the simulation process. Grid sensitivity is also evaluated using all grid levels.

When the solution is converged, appropriate local adaptation methods and strategies available from Fluent are performed on the coarse grid to better resolve the gradients and essential flow features. Various adaptation metrics are tested in an attempt to emulate the medium and fine grid solutions and justify the feasibility of using coarse grid plus adaptation approach to reduce computational resources.

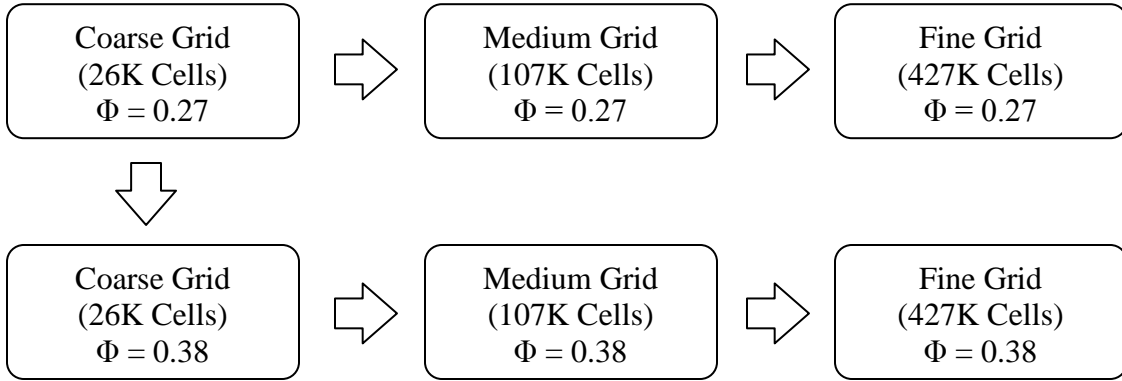


**Figure 7, Process of Simulation Runs**

Combustion efficiency is calculated and compared for all cases. The mass flow rate of water vapor at the exit plane of the extender-nozzle is used to calculate a form of combustion efficiency using Eqn 11 [7]. The oxidizer-fuel mass ratio (OF) for O<sub>2</sub>-H<sub>2</sub> is 8.

$$\eta_c = \frac{\dot{m}_{H_2O}}{\dot{m}_{H_2, injected} \cdot (1 + OF)} \quad (11)$$

## IV. Results

### A. $\Phi = 0.00$ (Fuel-off)

In order to simulate a fuel-off condition for the flowpath, the fuel injector nozzle was replaced by an isothermal wall with temperature of 1000K (in agreement with combustor wall temperature). Figure 8 shows the Mach number contours of the entire flowpath and the boundary layer captured and resolved near the wall. The top wall of the isolator is shown specifically. Figure 9 shows the flow features in the flowpath for different grids. The flow in the isolator reaches nearly Mach 2. An oblique shock is created as the flow is turned by the compression ramp. The shock is reflected off the bottom wall and propagates downstream through the combustor and extender nozzle. These shock structures caused the peaks and troughs in the static pressure plot in Figure 11. Note that all the pressure plots presented in this study are normalized by the reference pressure,  $P_{ref}$ , which was measured at the beginning of the isolator to be 43.3 kPa (in agreement with results from [6]). Grid convergence has been demonstrated as the pressure profile of the medium and fine grids matches closely. The flow is supersonic throughout the isolator, combustor and extender-nozzle in the absence of combustion. When the flow is expanded in the  $2.9^\circ$  extender-nozzle, it is accelerated to just above Mach 2 before separating from the top and bottom wall at  $X = 0.2$  m. However, the flow reattaches itself to the bottom wall at  $X = 0.25$  m due to not as strong an adverse pressure gradient as the top wall. A subsonic recirculation region exists in the combustor just aft of the compression ramp as shown by streamlines in Figure 10.



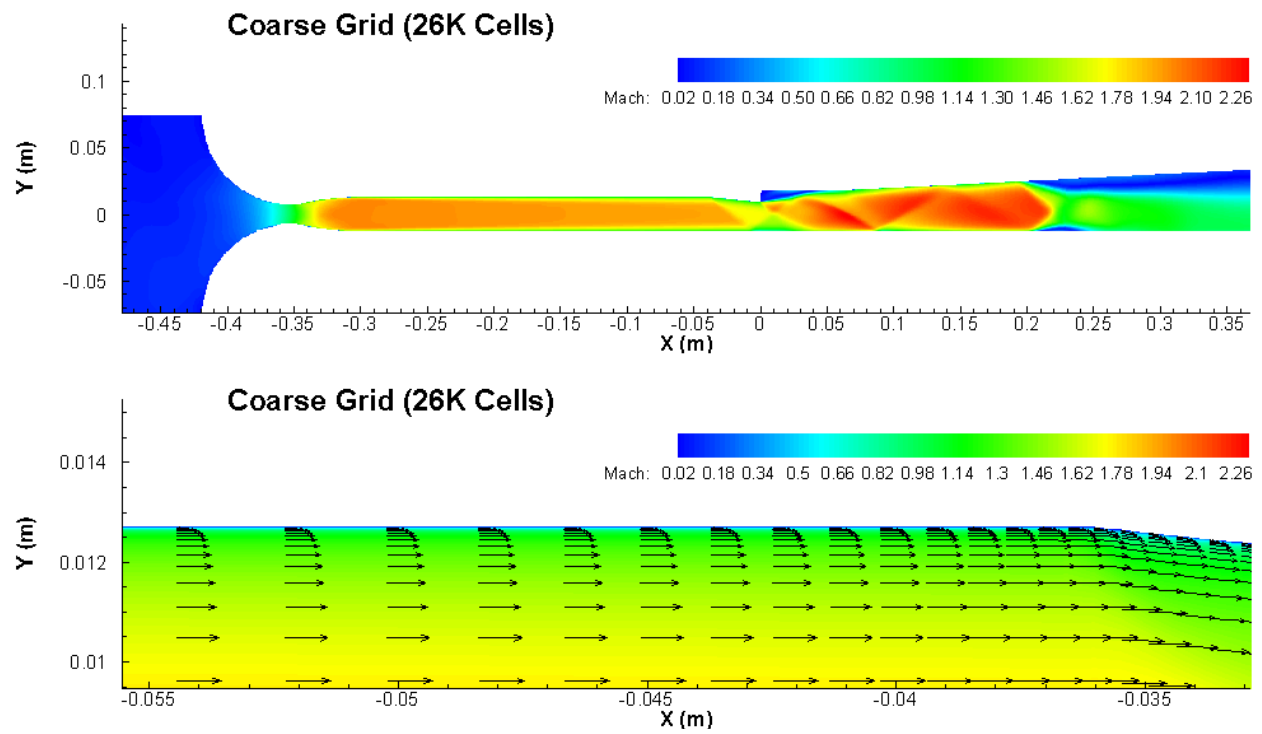


**Figure 8, Mach number Contours and Boundary Layer of Coarse Grid,  $\Phi = 0.00$  (Fuel-Off)**

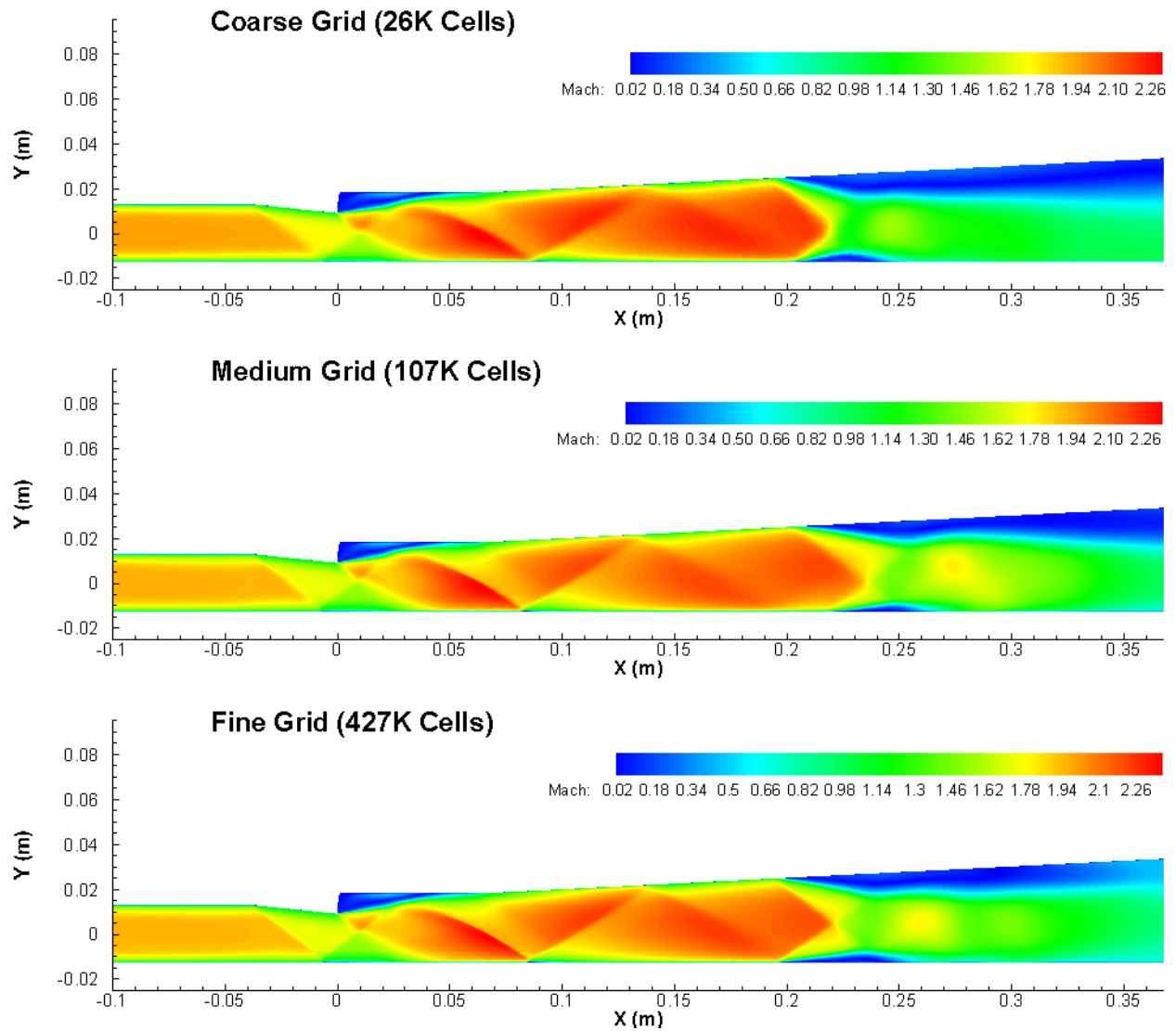


**Figure 9, Mach number Contours of Coarse, Medium, and Fine Grid,  $\Phi = 0.00$  (Fuel-Off)**

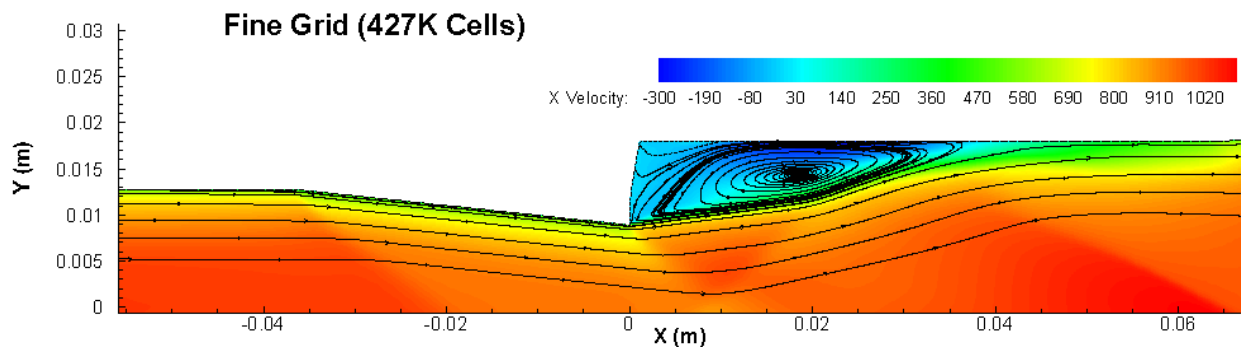


**Figure 10, Axial Velocity Contours and Streamlines within Isolator-Combustor,  $\Phi = 0.00$  (Fuel-Off)**

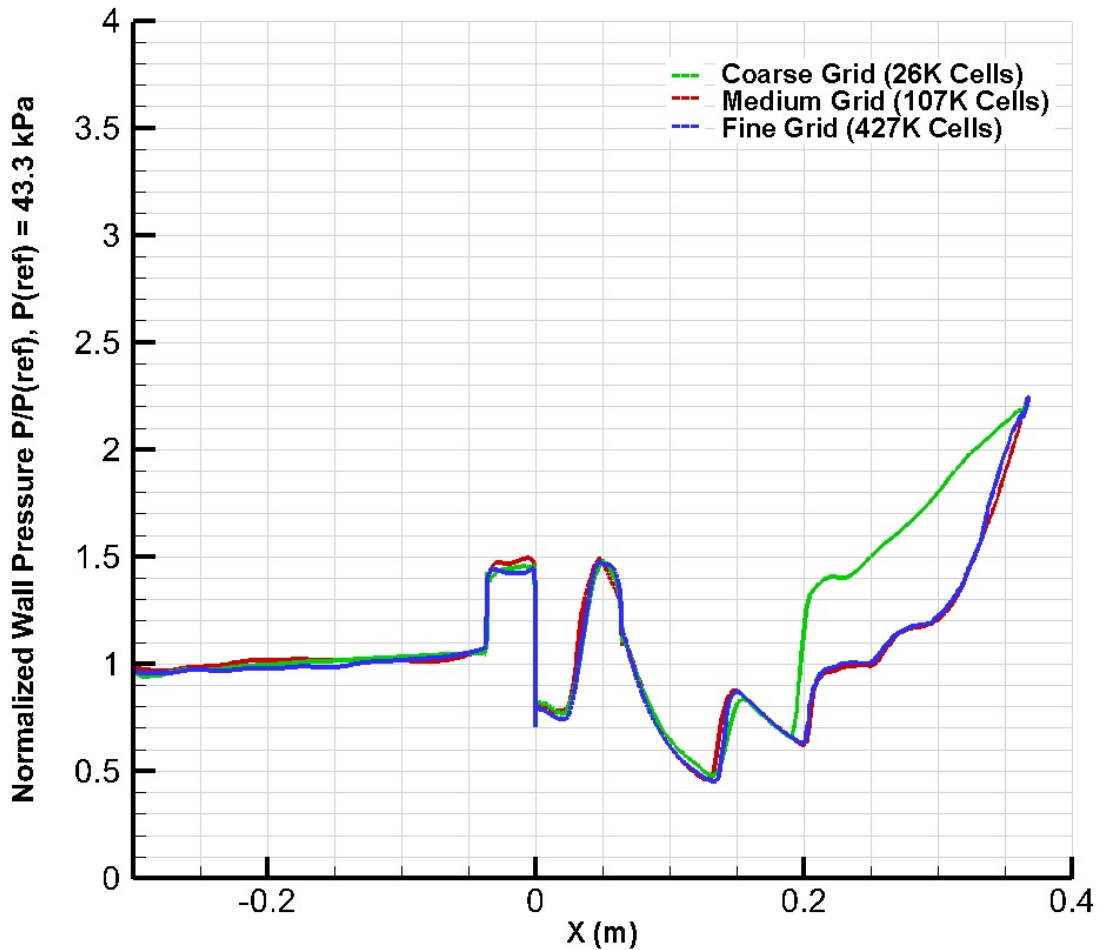


**Figure 11, Static Pressure Distribution along Fuel Injector Wall: Coarse, Medium, and Fine Grid Comparison,  $\Phi = 0.00$  (Fuel-Off)**

**B.  $\Phi = 0.27$**

Figure, 12, 13 and 14 show the Mach number, mass fraction of H<sub>2</sub>O and static temperature contours of the flowpath at  $\Phi = 0.27$  with the coarse, medium, and fine grid. In coarse and medium grid, the hydrogen fuel mixes with the air from the core flow and starts to combust before reaching the extender-nozzle. Water vapor diffuses downstream and away from the fuel injector wall. High temperatures of up to 2520 K are present near the extender-nozzle

wall. The Mach number contours show that the oblique shock from the compression ramp is reflected off the bottom wall and the reacting flow at the top wall; creating several distinct regions of high speed flow which decreases in velocity from the combustor to the outlet of the extender-nozzle. As most of the air entering the combustor is supersonic, the combustor is operating in scramjet mode. In fine grid however, the solution is significantly different. A supersonic region with Mach numbers up to 2.2 is present in the combustor but combustion starts to occur only at the extender-nozzle. In an attempt to solve the unknown cause of discrepancy in solution, the fuel is 'numerically' ignited again for the fine grid. However, the same solution is obtained. Further investigation of this matter is presented in the following sections with higher equivalence ratio.

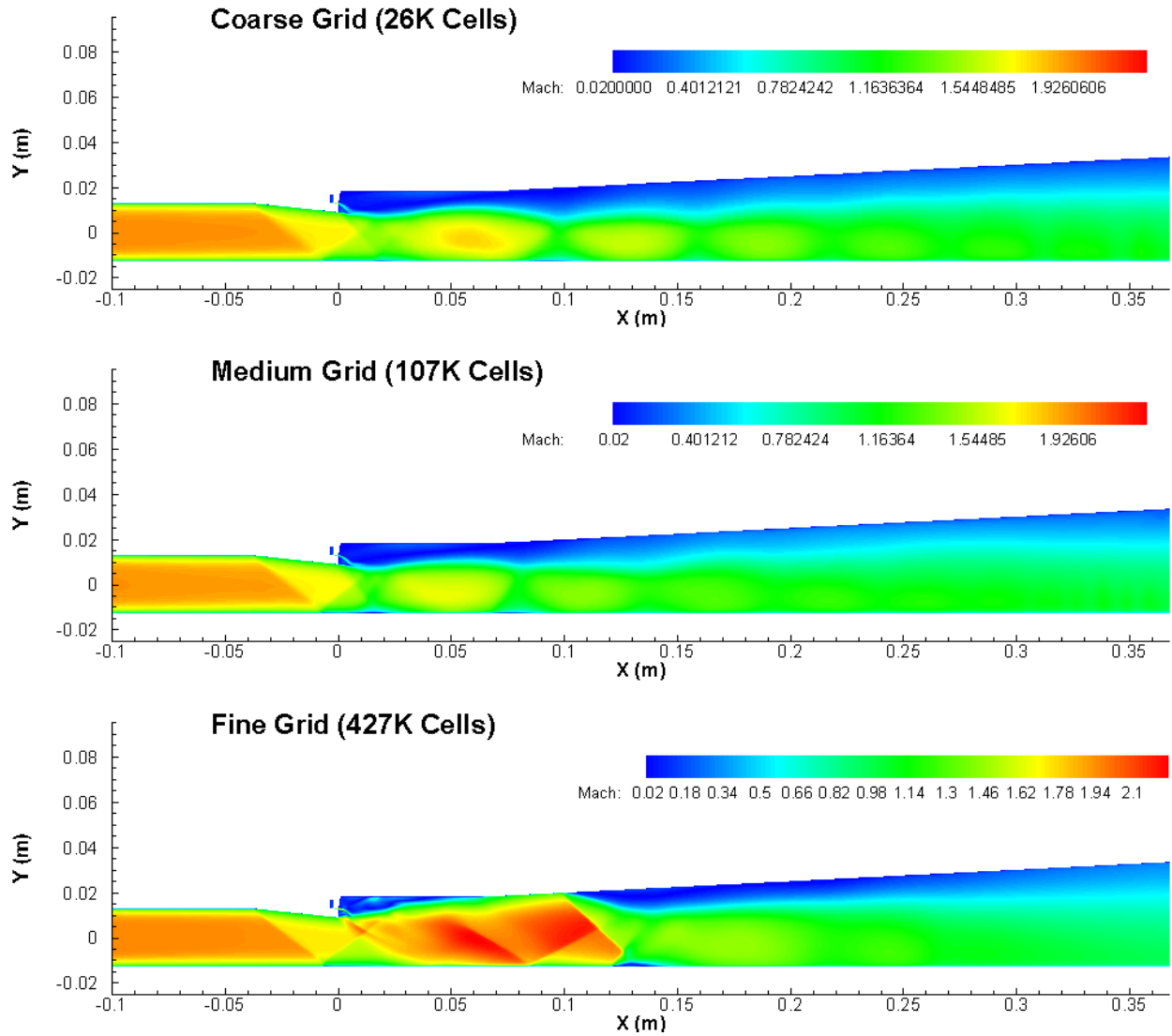


**Figure 12, Mach number Contours of Coarse, Medium, and Fine Grid,  $\Phi = 0.27$**

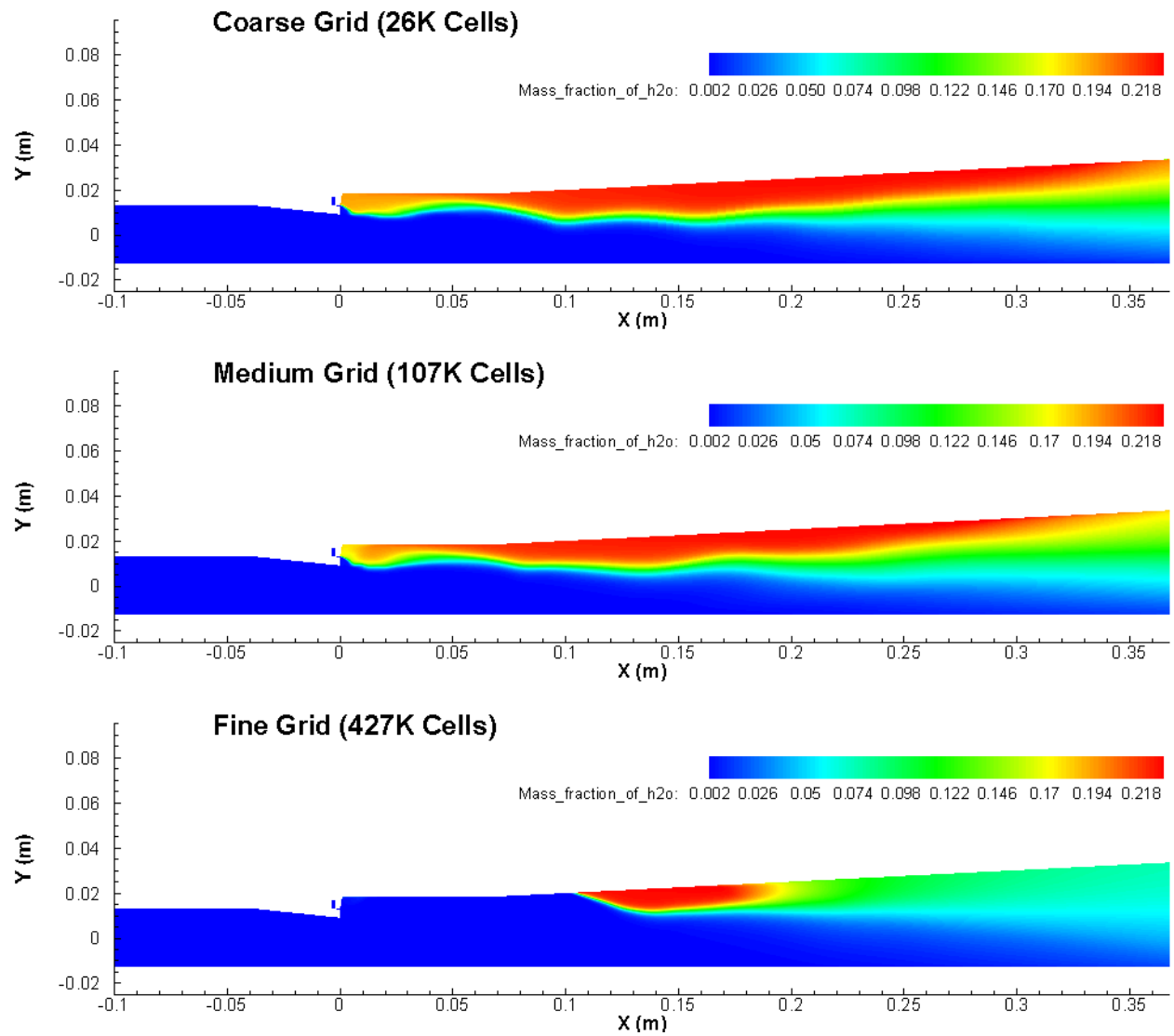


**Figure 13, Mass Fraction of H<sub>2</sub>O Contours of Coarse, Medium, and Fine Grid,  $\Phi = 0.27$**

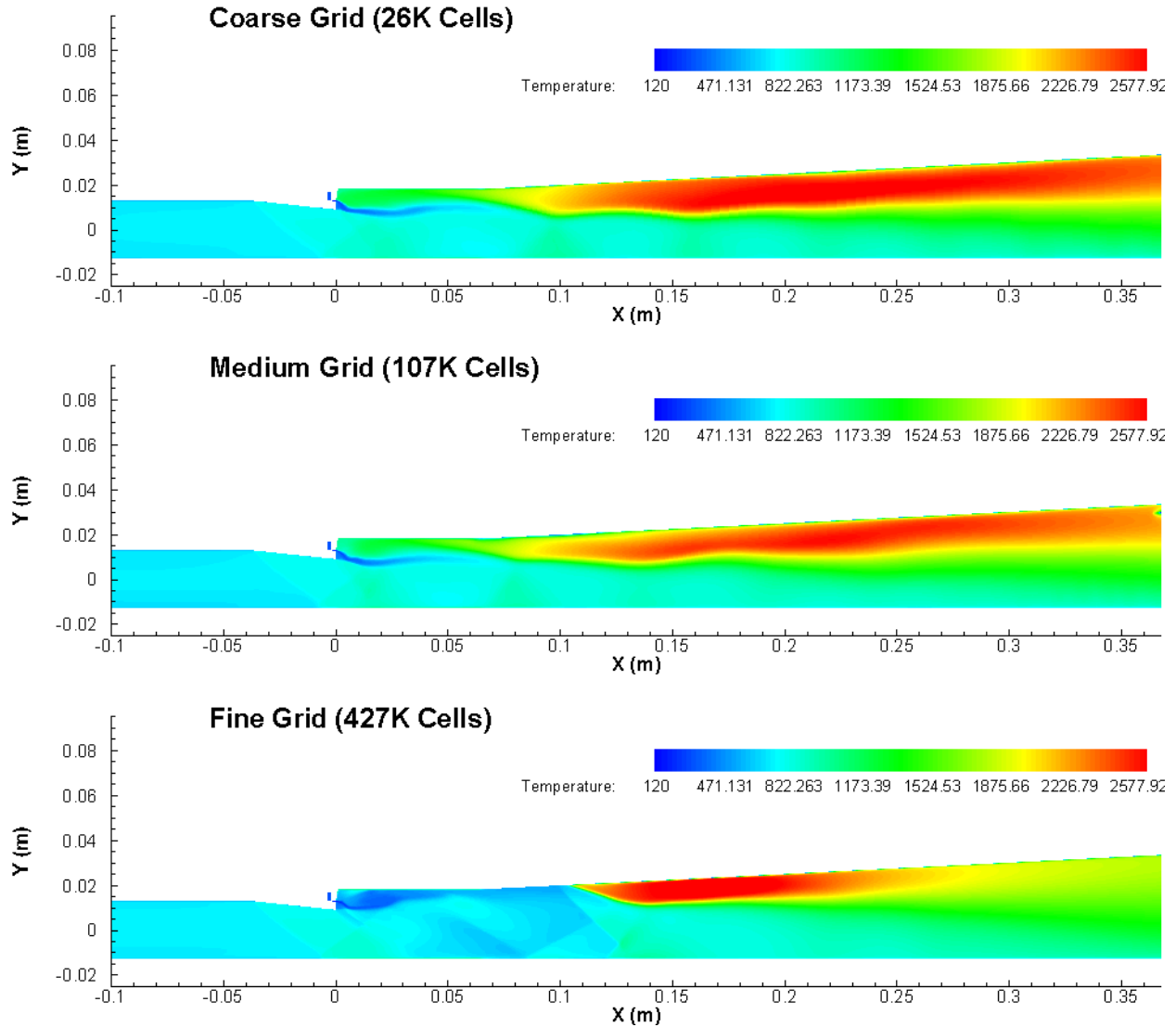


**Figure 14, Static Temperature Contours of Coarse, Medium, and Fine Grid,  $\Phi = 0.27$**

The static pressure distribution of the flowpath is shown in Figure 15 for different grids at  $\Phi = 0.27$ . In the isolator, the static pressure distribution is similar for all grid levels. In the combustor and extender-nozzle however, the coarse grid gives a lower pressure profile. Besides having a lower peak combustor static pressure, the coarse grid also gives a lower combustion efficiency compared to the medium grid solution. The fine grid gives a lower pressure profile at the combustor as there is essentially no combustion taking place upstream of the extender-

nozzle. Combustion efficiency is also lower compared to coarse and medium grid. A comparison of these parameters is shown in the Grid Adaptation Sensitivity Study section. Figure 16 shows the convergence history of water vapor mass fraction at the exit plane.

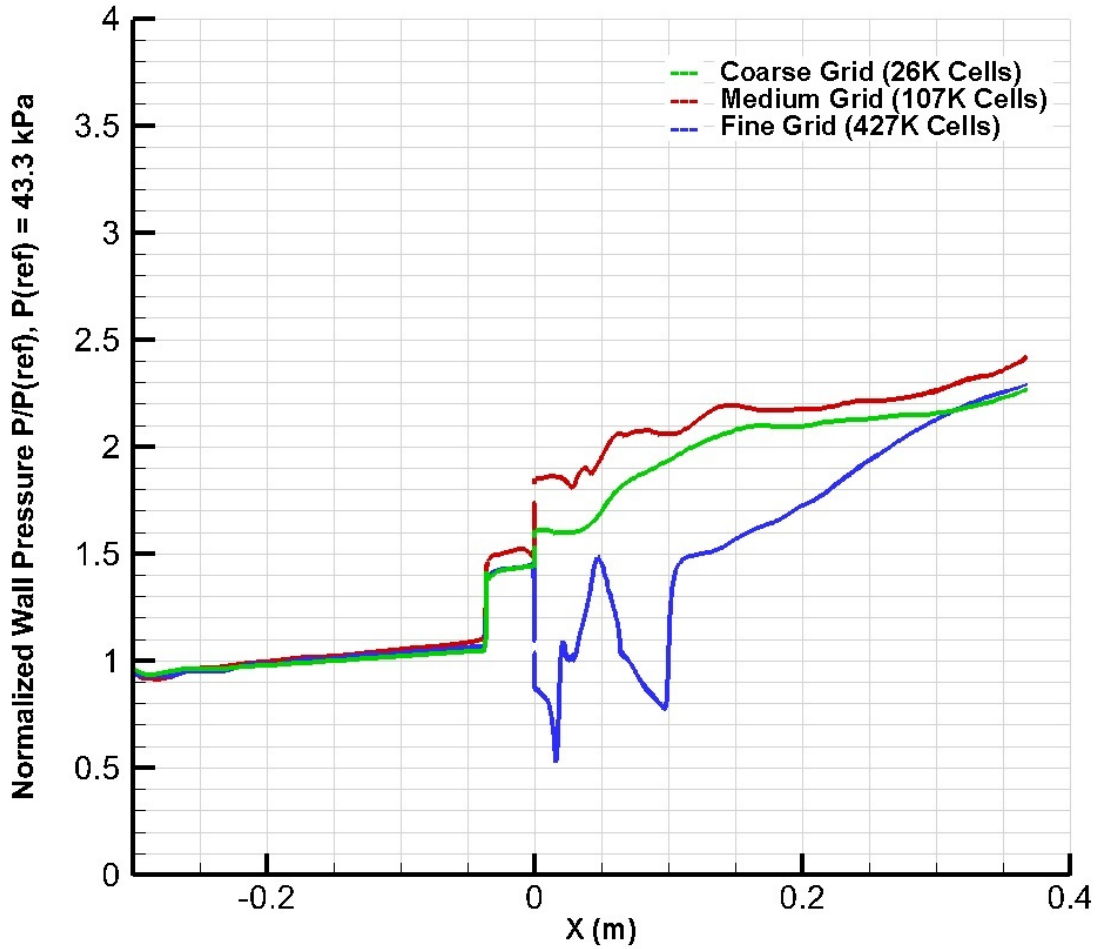
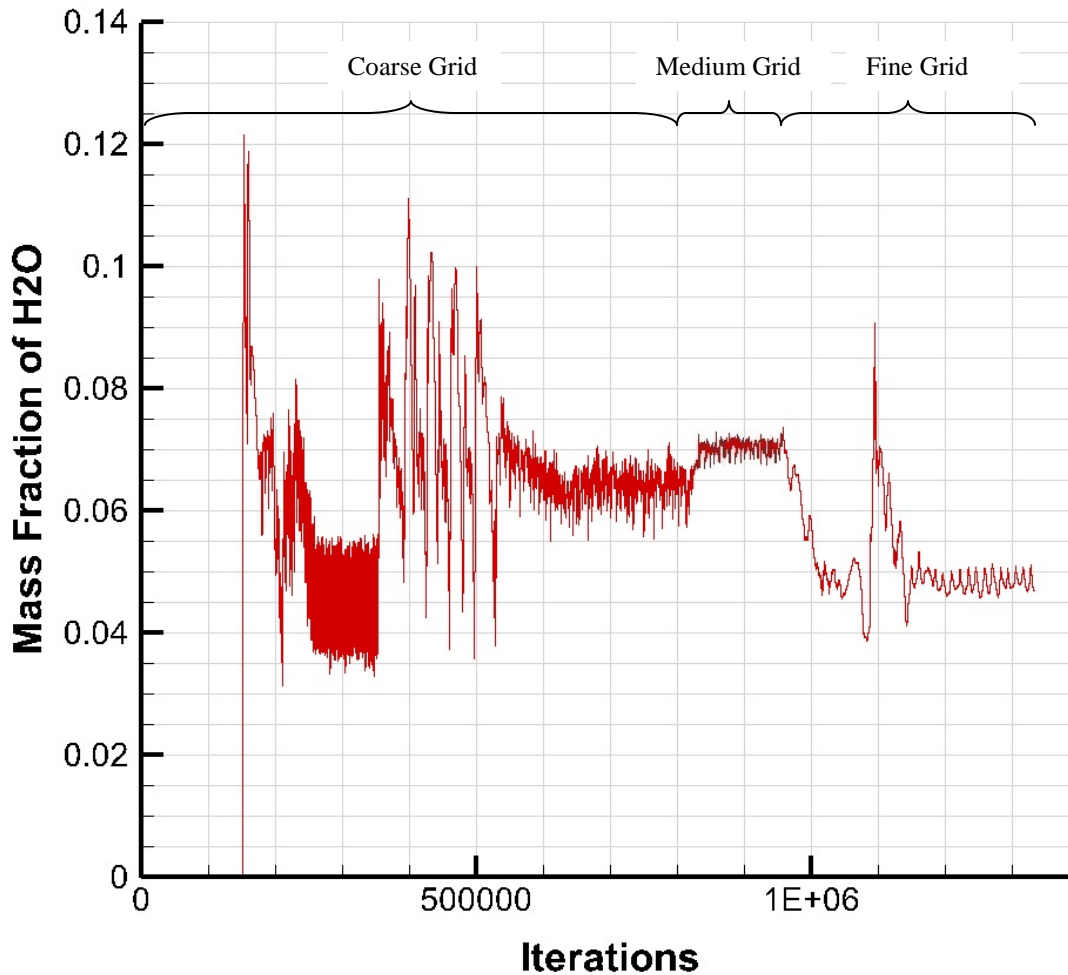


Figure 15, Static Pressure Distribution along Fuel Injector Wall: Coarse, Medium, and Fine Grid Comparison,  $\Phi = 0.27$



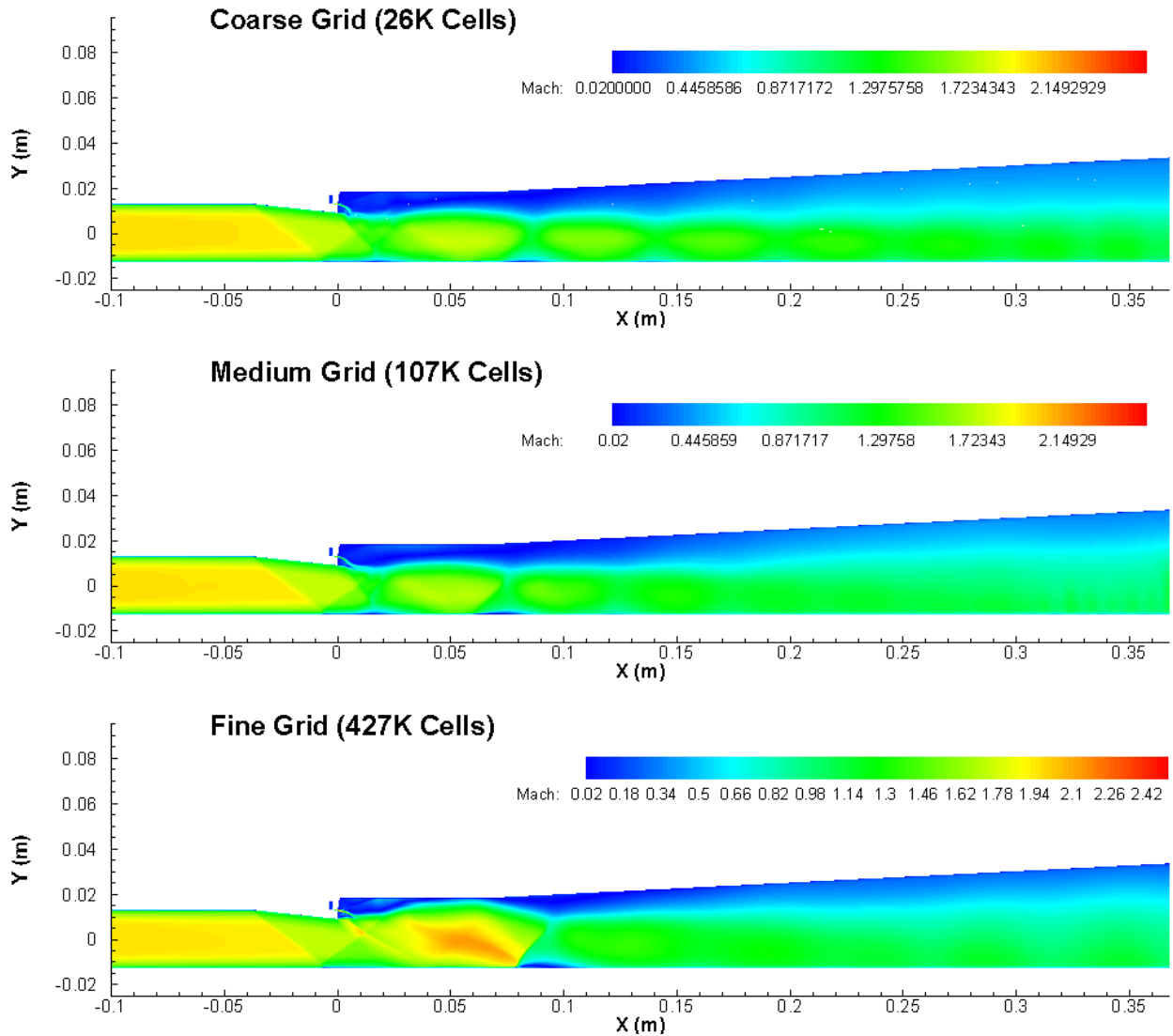


**Figure 16, Convergence History of Water Vapor at Exit Plane,  $\Phi = 0.27$**

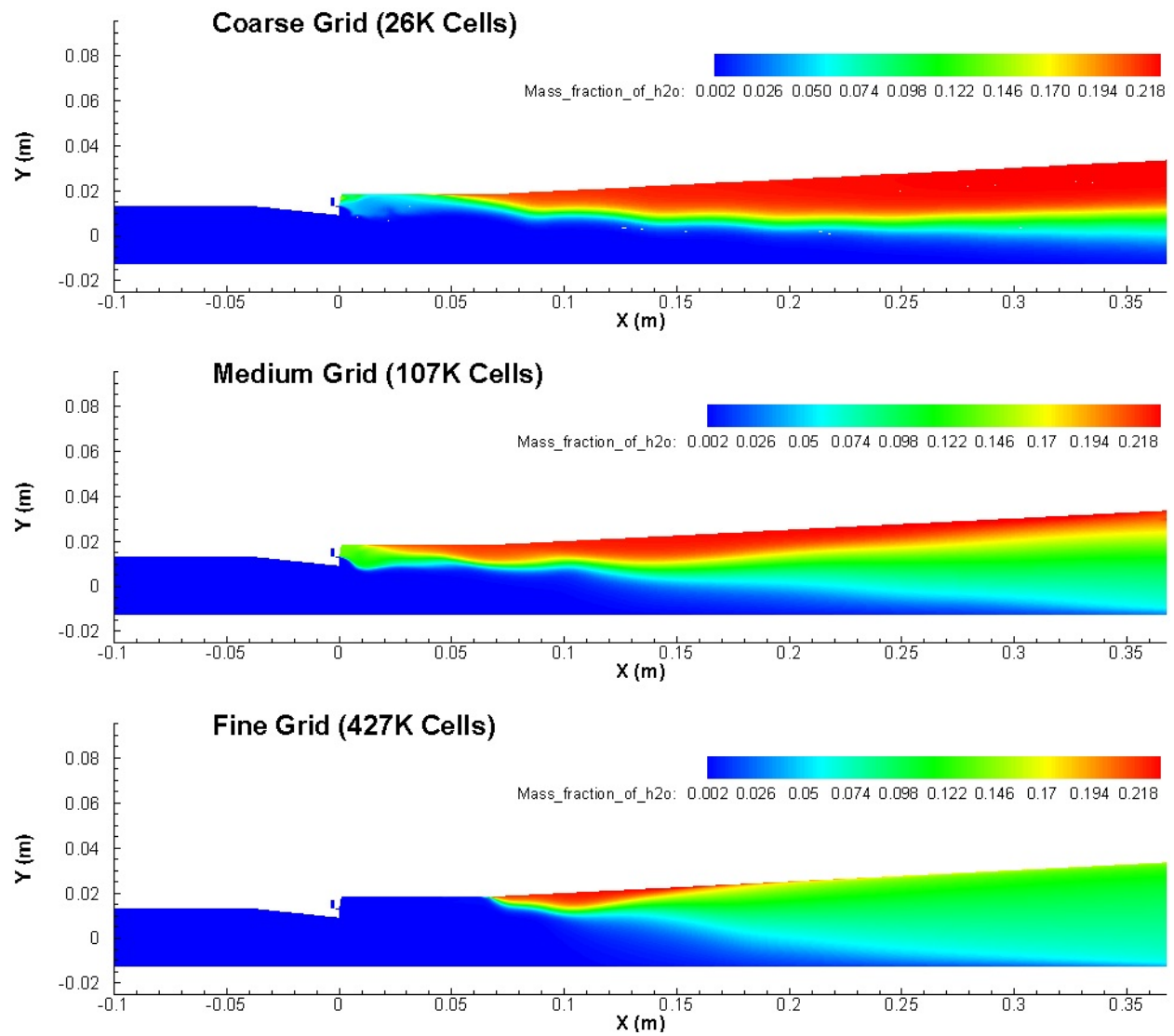
**C.  $\Phi = 0.38$**

Figure 17, 18 and 19 show the different grid solutions at  $\Phi = 0.38$ . As with the coarse and medium grid at  $\Phi = 0.27$  cases, combustion begins at the combustor and is sustained throughout the extender-nozzle. With more hydrogen fuel being burned, temperature in the extender nozzle reached as high as 2720 K. Note that in the coarse grid solution, less combustion is occurring in the combustor. At a higher equivalence ratio, it is suspected that the shear layer between the hydrogen fuel and the core flow is not sufficiently resolved due to lack of cells. The lower

combustion in the combustor section of the coarse grid is accountable for the difference in water vapor mass fraction and static temperature distribution, compared to the medium grid solution. As most of the air entering the combustor is still supersonic, the combustor is operating at scramjet mode. The flow features of the fine grid solution are different from the coarse and medium grid, including a more well-defined shock pattern within combustor. Combustion occurs aft of the supersonic region of the combustor for the fine grid solution. This issue is further investigated in the following section.



**Figure 17, Mach number Contours of Coarse, Medium, and Fine Grid,  $\Phi = 0.38$**



**Figure 18, Mass Fraction of H<sub>2</sub>O Contours of Coarse, Medium, and Fine Grid,  
 $\Phi = 0.38$**

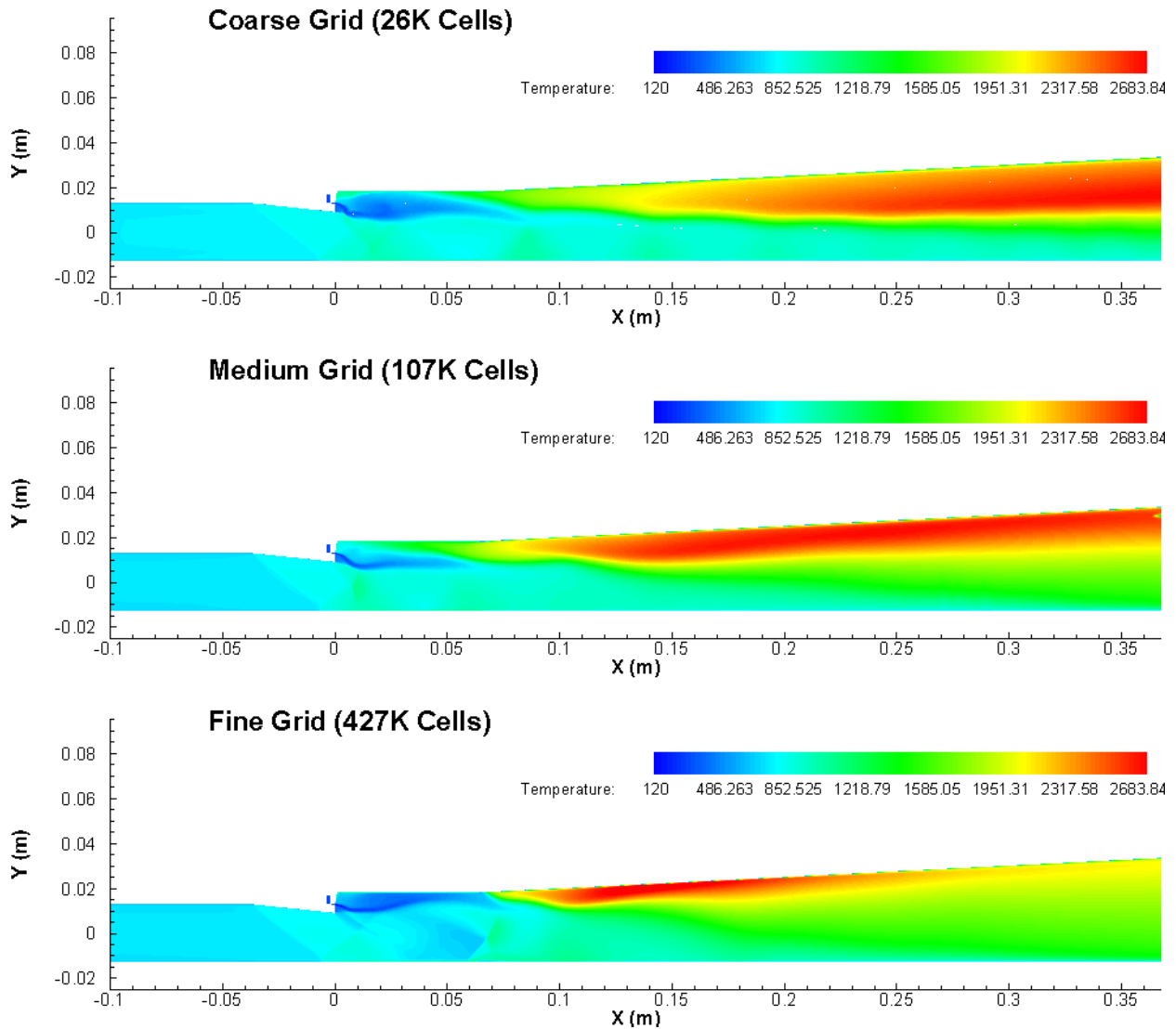


**Figure 19, Static Temperature Contours of Coarse, Medium, and Fine Grid,  $\Phi = 0.38$**

Figure 20 shows the static pressure distribution in the flowpath for different grids at  $\Phi = 0.38$ . The coarse grid gives a lower pressure profile at the combustor and extender-nozzle compared to the medium grid. Peak combustor static pressure and combustion efficiency are also lower. The fine grid gives a lower pressure profile at the combustor but yields a higher pressure at the extender-nozzle as combustion starts occurring. Combustion efficiencies between different grids are compared in the Grid Adaptation Sensitivity Study section. Figure 21 shows the

convergence history of water vapor mass fraction at the exit plane. Note the increase in water vapor mass fraction as the equivalence ratio is increased from 0.27 to 0.38.

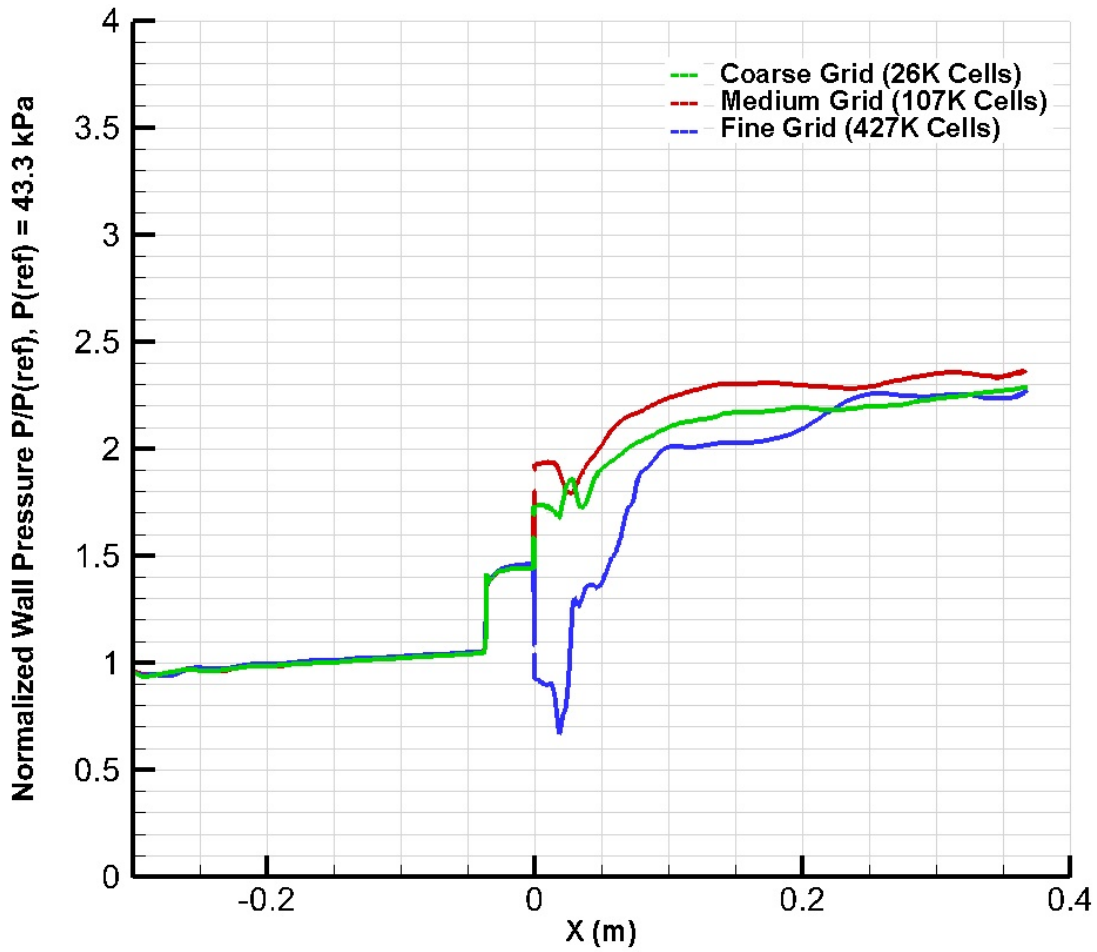
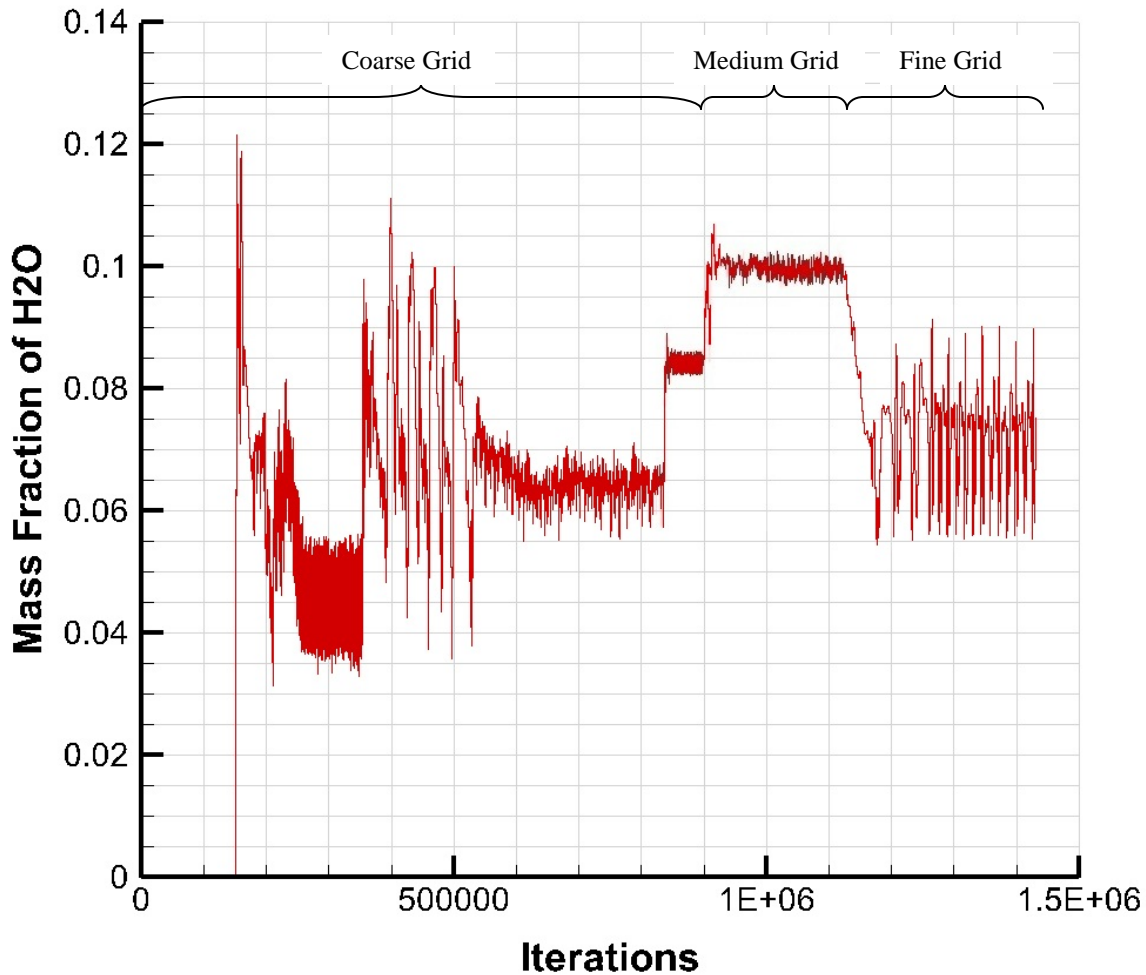


Figure 20, Static Pressure Distribution along Fuel Injector Wall: Coarse, Medium, and Fine Grid Comparison,  $\Phi = 0.38$



**Figure 21, Convergence History of Water Vapor at Exit Plane, Fine Grid,  $\Phi = 0.38$**

**D.  $\Phi = 0.38$  (Transient)**

The fine grid solution was found to be different from coarse and medium grid at equivalence ratios of 0.27 and 0.38. Attempts to resolve this issue by reigniting the fuel did not result in any change in the fine grid solutions. Hence, it is speculated that this discrepancy in solution was due to path dependency. When the medium grid was refined globally, extrapolated values might have numerically created a significant perturbation in the solution which is not ‘recoverable’ and drove the simulation to having a different solution. To examine this theory, a

time-accurate simulation was performed for the case of  $\Phi = 0.38$ . The medium grid was refined globally and ran using transient analysis. A time-step of  $1e^{-4}$  s was used with a maximum number of 20 iterations per time-step. The results are shown in the following discussion.

Figure 22 shows the Mach number contours at increasing physical time of 0 second (when the medium grid was refined globally and transient analysis began) to 1.74 seconds. As time increases, it can be observed that the supersonic flow region in the combustor is increasing in size and speed. At  $t = 0.87$  s, reflected shocks are formed at the top and bottom wall at  $x = 0.08$  m. Flow separation occurs aft of the reflected shocks. At  $t = 1.74$  s, the reflected shocks have moved upstream to  $x = 0.07$  m and the flow has achieved steady state. The flow aft of the reflected shocks remains supersonic while gradually decreasing to high subsonic speeds. From  $t = 1.74$  s onwards the solution was found to be similar to the steady-state simulation from previous sections.

Figure 23 shows the mass fraction of H<sub>2</sub>O contours at the same time frames. At  $t = 0.44$  s, as the supersonic region grows in the combustor, combustion is hindered and flame is diminishing in the combustor region. At  $t = 0.87$  s, combustion is mostly occurring aft of the reflected shocks at  $x = 0.08$  m and is almost extinguished in the combustor. At  $t = 1.74$  s, no combustion takes place in the combustor. A steady-state is achieved and combustion occurs aft of the reflected shocks at  $x = 0.07$  m. Combustion efficiency has dropped significantly compared to coarse and medium grid solutions.

Figure 24 shows the static pressure contours at the same time frames. At  $t = 0$  s, high pressure regions can be seen behind the reflected shocks which originate from the compression ramp. As the supersonic region grows, from  $t = 0$  s to  $t = 0.44$  s, the shock structures downstream of the compression ramp changes. High pressure region occurs behind the reflected shocks at  $x =$

0.1 m. At  $t = 1.74$  s, steady-state solution is achieved and a static pressure of  $\sim 100$  kPa is observed behind the intersecting reflected shocks at  $x = 0.9$  m. The static pressure in the combustor is significantly lower compared to coarse and medium grid solutions due to the lack of combustion. Where combustion used to occur is now essentially a supersonic flow region with Mach number up to 1.7.

Time-accurate solutions were found to be similar to steady-state solutions using fine grids. This result ruled out the speculation of path-dependency to be the cause of different solutions between medium and fine grid. Note that this issue was not present in the fuel-off case, where grid convergence was achieved, as shown in Figure 9. With limited resources, it is speculated that the unique change in fine grid solution could be due to shock-boundary layer interactions. In the fine grid, the laminar sublayer and boundary layer profiles are better resolved as the mesh near the walls is very dense, with wall  $y^+$  values of less than 1. In combination with well resolved shocks and pressure gradients, the points at which shocks impinge on the walls might be better resolved. This could contribute to an impact on the boundary layer profile of the top wall of the combustor and extender-nozzle, which consequently affects the flow features in the combustor and the flow separation in the extender nozzle.



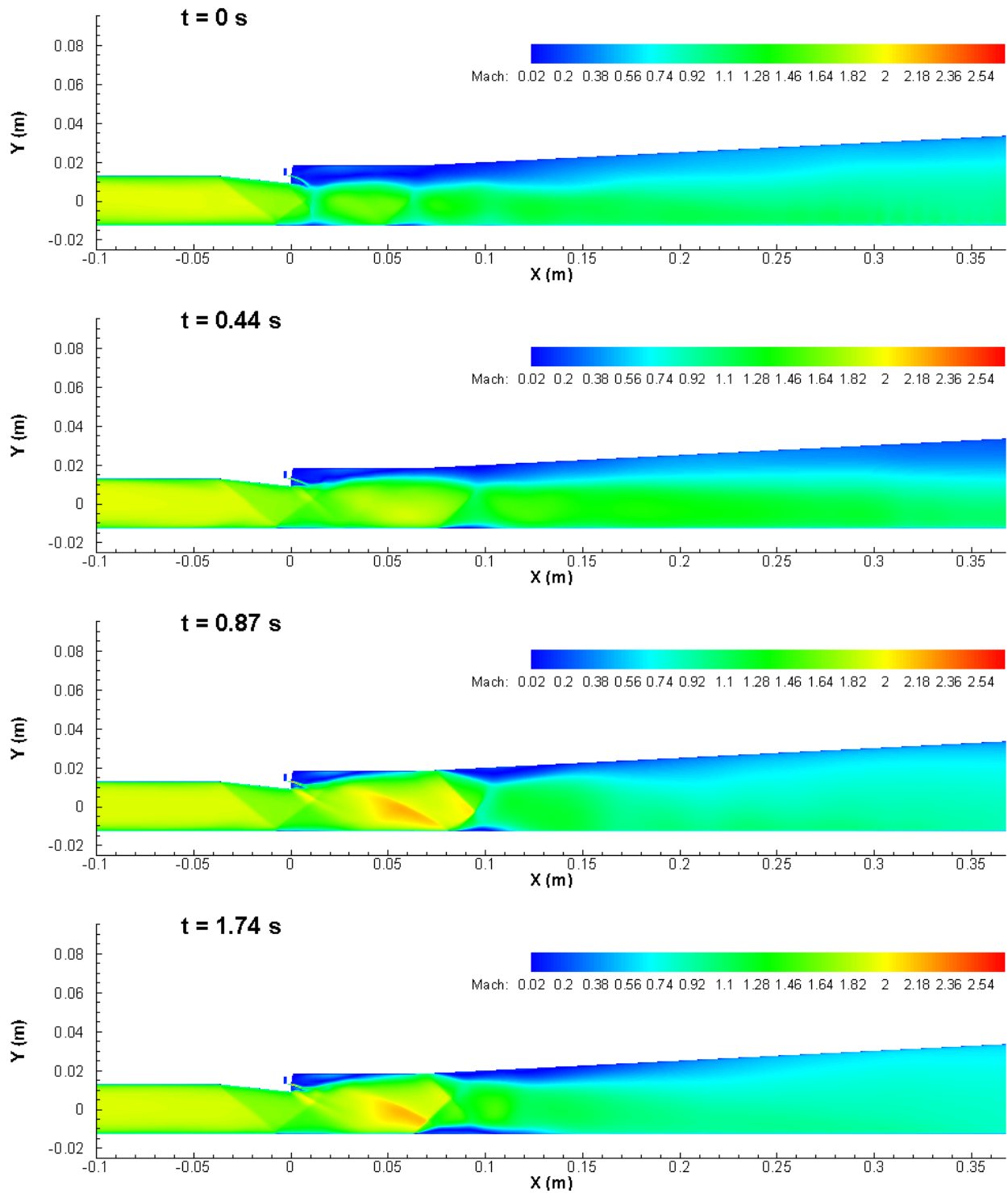
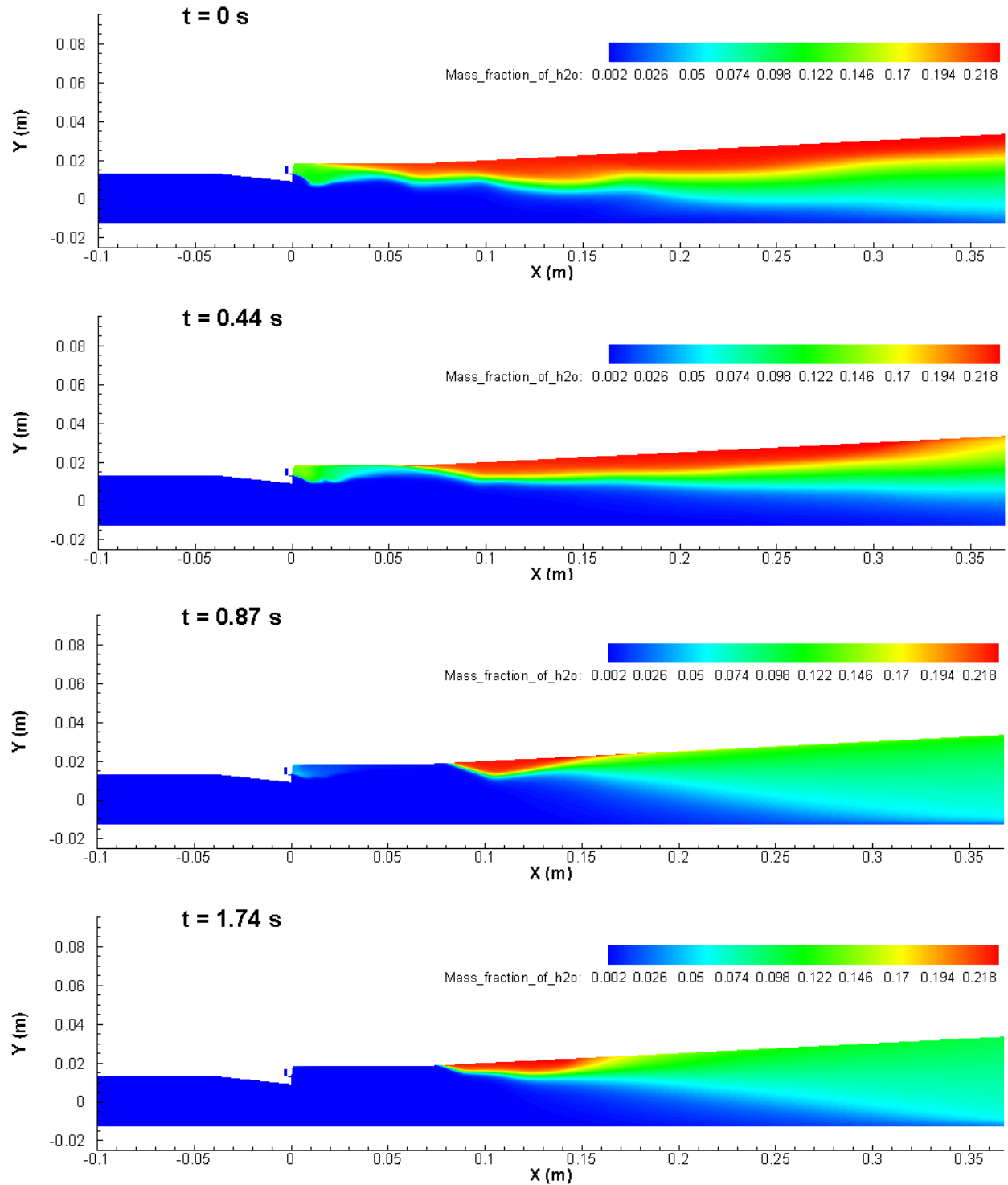
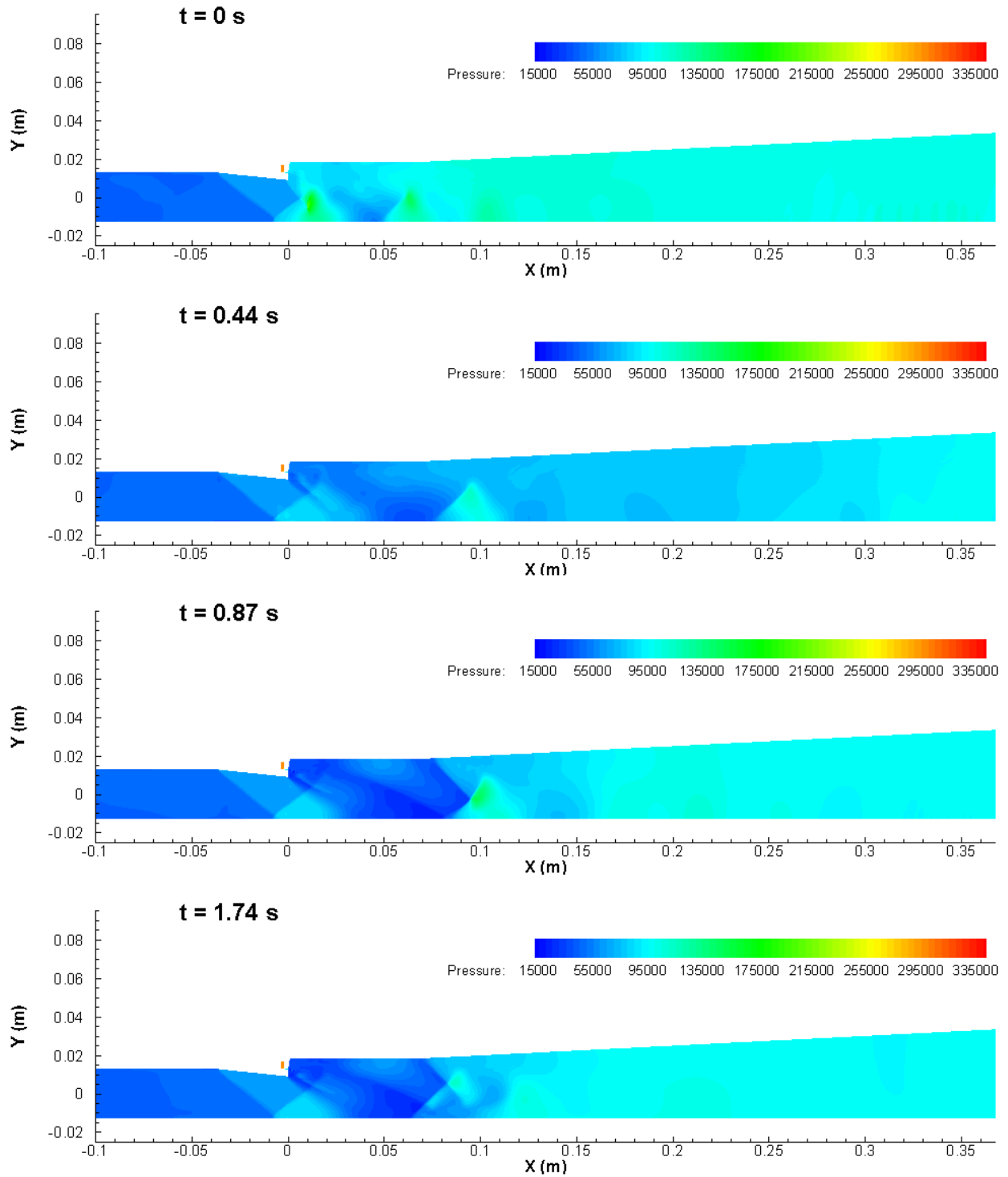


Figure 22, Mach number Contours of Fine Grid,  $\Phi = 0.38$



**Figure 23, Mass Fraction of H2O Contours of Fine Grid,  $\Phi = 0.38$**



**Figure 24, Static Pressure Contours of Fine Grid,  $\Phi = 0.38$**

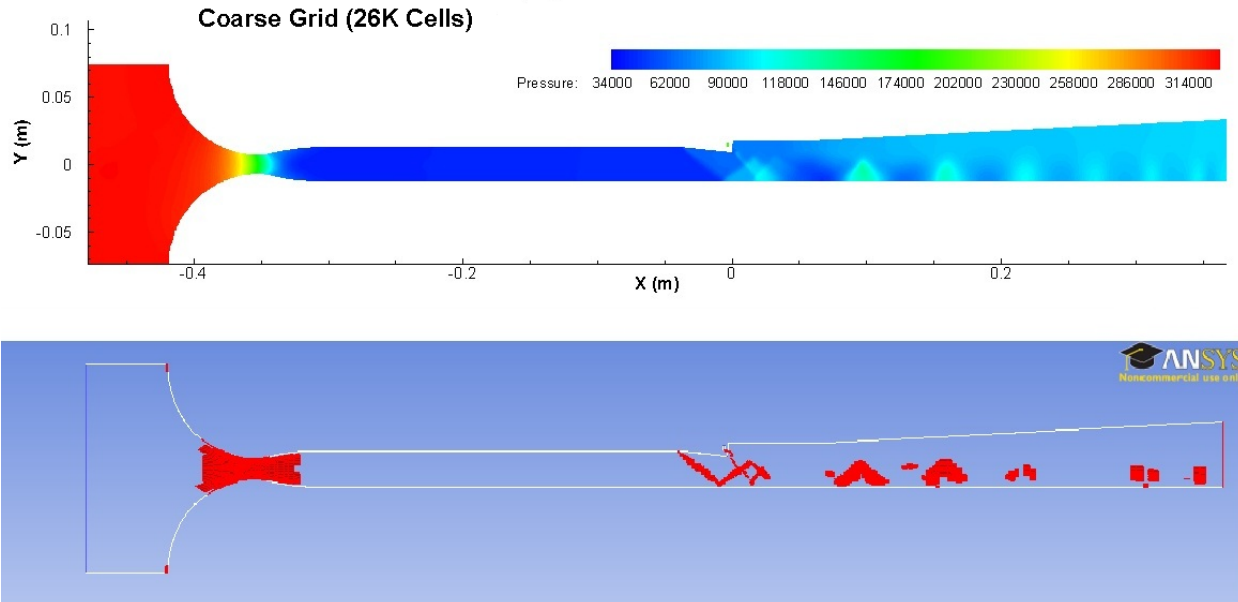
## V. Grid Adaptation Sensitivity Study

Different adaptation methods are explored to enhance the solution of the coarse grid and to determine the effectiveness of grid adaptation. Adaptation based on gradients and curvatures of mass fraction of H<sub>2</sub>O, static pressure, static temperature, turbulent kinetic energy and turbulent dissipation rate have been selected for this study as these fields are crucial in high speed reacting flow simulations. Region based adaptation is also explored. For the latter method, the grid at different rectangular regions in the combustor is adapted: 1) upper combustor section aft of the compression ramp and, 2) entire combustor. The combustor section was chosen for region adaptation in hopes that refining the grid at the area will better resolve the mixing shear layer of the hydrogen fuel and air.

When the original coarse grid solution is converged, adaptation based on different parameters is performed and the refine threshold is set such that 25 percent of cells will be added to the original grid. Table 2 provides a matrix of numerical simulations for this exploration. The metrics for evaluating adaptation effectiveness include the combustion efficiency, peak static pressure in the combustor, and cell usage.

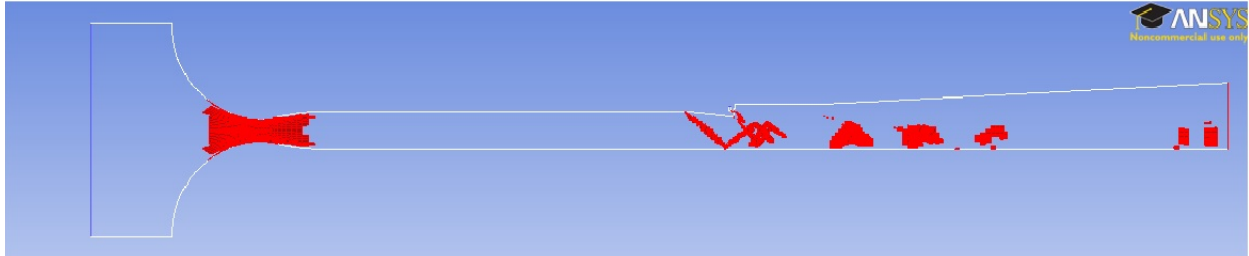
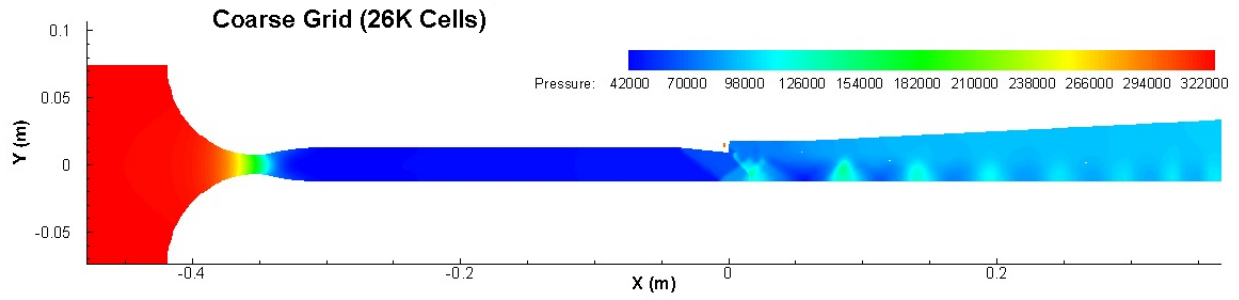
It was found that adaptation based on static pressure gradient yields the best results compared to other parameters and methods. Regions in the original coarse grid with high pressure gradients were refined and better resolved. Adapted solutions were closer to that of the medium grid. Figure 25 shows the static pressure contour of the flowpath and the adapted regions at  $\Phi = 0.27$ . High static pressure gradients can be observed at the oblique shock formed by the compression ramp, and the reflected shocks that propagate downstream to the extender nozzle. These regions are refined to yield the following solutions.

Figure 27 shows the static pressure distribution along the fuel injector wall from the compression ramp to the extender-nozzle for  $\Phi = 0.27$ . Although still not exactly the same, the adapted coarse grid clearly gives a significant improvement and better match to the medium grid results in the combustor section. However, the static pressure distribution in the extender nozzle is over predicted. The combustion efficiency is also increased to 100 percent from 95 percent, which matches the medium grid solution. It should be noted that further adaptation based on static pressure gradient was performed and no notable improvement in solution was obtained. Hence, local adaptation did not give a solution similar to that of the fine grid. At  $\Phi = 0.27$ , other adaptation methods prove to have no significant improvement in static pressure distribution and combustion efficiency. Static pressure curvature and static temperature gradient adaptations give worse results than the original coarse grid. Some prevalent flow features and their locations might not be sufficiently resolved in the coarse grid. When the grid is refined in the incorrect location, the global error of the solution is not reduced. Hence, the adapted solution may be no better than the original solution, and in fact, may yield an incorrect solution [14].



**Figure 25, Static Pressure Contour and Adapted Regions based on Static Pressure Gradient,  $\Phi = 0.27$**

At  $\Phi = 0.38$ , adaptation based on static pressure gradient also gives better results than other parameters and methods. However, the improvement is not as prominent. Figure 26 shows the static pressure contour of the flowpath and the adapted regions at  $\Phi = 0.38$ . Figure 28 shows the static pressure distribution comparison. It can be seen that the adapted coarse grid yields better resemblance to the medium grid result in the combustor, but the pressure profile is still under predicted. Combustion efficiency increased from 85 to 90 percent, falling short of the medium grid solution of 98 percent. The decrease in improvement over the adapted grid could be due to rise in turbulent kinetic energy levels in the injector plume (from higher fuel mass flow rate) which are not resolved sufficiently. Further adaptation based on static pressure gradient was carried out without any improvement in solution. Other parameters and methods give worst or no improvement in solution.



**Figure 26, Static Pressure Contour and Adapted Regions based on Static Pressure Gradient,  $\Phi = 0.38$**

**Table 2, Matrix of Adaptation Simulations at Different Equivalence Ratios**

<b>Equivalence Ratio, <math>\Phi</math></b>	<b>Grid F – 427K Cells M – 107K Cells C – 26K Cells</b>	<b>Adaptation Method</b>	<b>Percentage of Cells Added (%)</b>	<b>Combustion Efficiency, <math>\eta</math> (%)</b>	<b>Peak Combustor Static Pressure, P (kPa)</b>
0.00	F	---	---	---	65
	M	---	---	---	65
	C	---	---	---	65
0.27	F	---	---	75	65
	M	---	---	100	90
	C	---	---	95	79
	C	Mass Fraction of H2O Gradient	25	95	79
		Mass Fraction of H2O Curvature		95	79
		Static Pressure Gradient		100	88
		Static Pressure Curvature		92	81
		Static Temperature Gradient		93	80
		Static Temperature Curvature		97	82
		Turbulent Kinetic Energy Gradient		95	80
		Turbulent Kinetic Energy Curvature		95	80
		Turbulent Dissipation Rate Gradient		95	79
		Turbulent Dissipation Rate Curvature		95	79
		Region (Upper Combustor Section)		95	79
Region (Entire Combustor Section)	62	95	79		



0.38	F	---	---	75	81	
	M	---	---	98	92	
	C	---	---	85	86	
	C	Mass Fraction of H2O Gradient	25		80	85
		Mass Fraction of H2O Curvature			80	84
		Static Pressure Gradient			90	87
		Static Pressure Curvature			85	85
		Static Temperature Gradient			85	86
		Static Temperature Curvature			85	86
		Turbulent Kinetic Energy Gradient			80	85
		Turbulent Kinetic Energy Curvature			80	85
		Turbulent Dissipation Rate Gradient			83	84
		Turbulent Dissipation Rate Curvature			80	83
	Region (Upper Combustor Section)			80	84	
Region (Entire Combustor Section)	78		84	85		

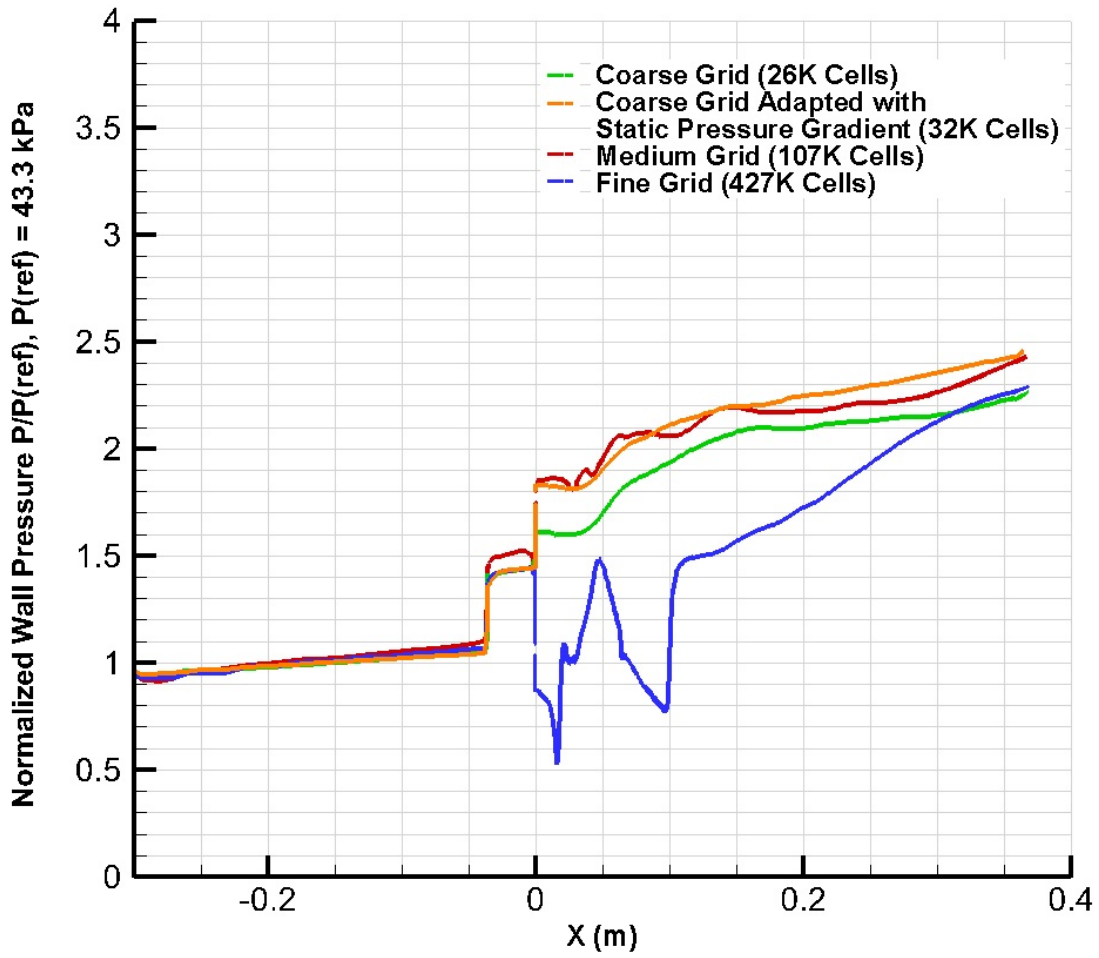


**Figure 27, Static Pressure Distribution along Fuel Injector Wall: Coarse, Medium, Fine, and Adapted Coarse Grid (based on Static Pressure Gradient) Comparison,  $\Phi = 0.27$**

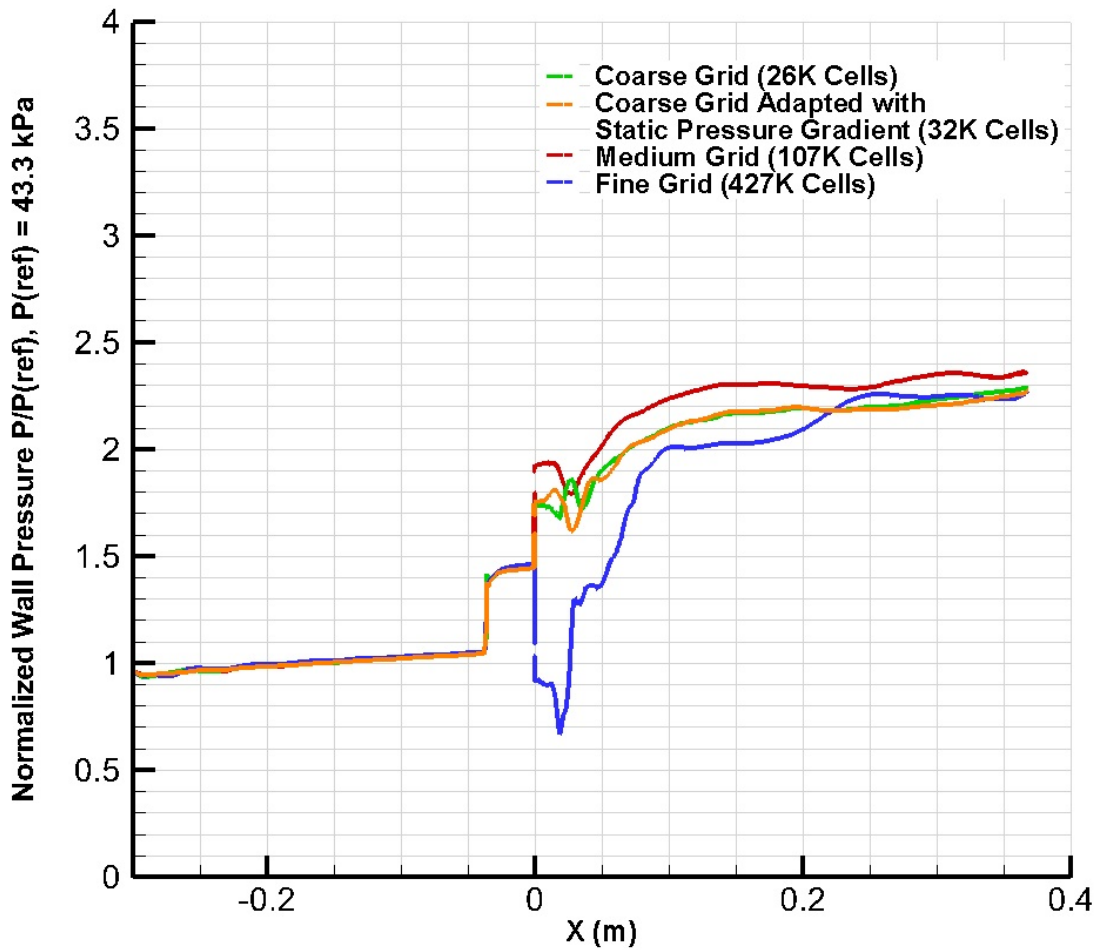


**Figure 28, Static Pressure Distribution along Fuel Injector Wall: Coarse, Medium, Fine, and Adapted Coarse Grid (based on Static Pressure Gradient) Comparison,  $\Phi = 0.38$**

Figure 29 and 30 show the convergence history of water vapor mass fraction at the exit plane of the flowpath. At  $\Phi = 0.27$ , notable increase in water vapor mass flux can be observed after the grid is adapted based on static pressure gradient. In the case of  $\Phi = 0.38$ , the increase is relatively minimal.

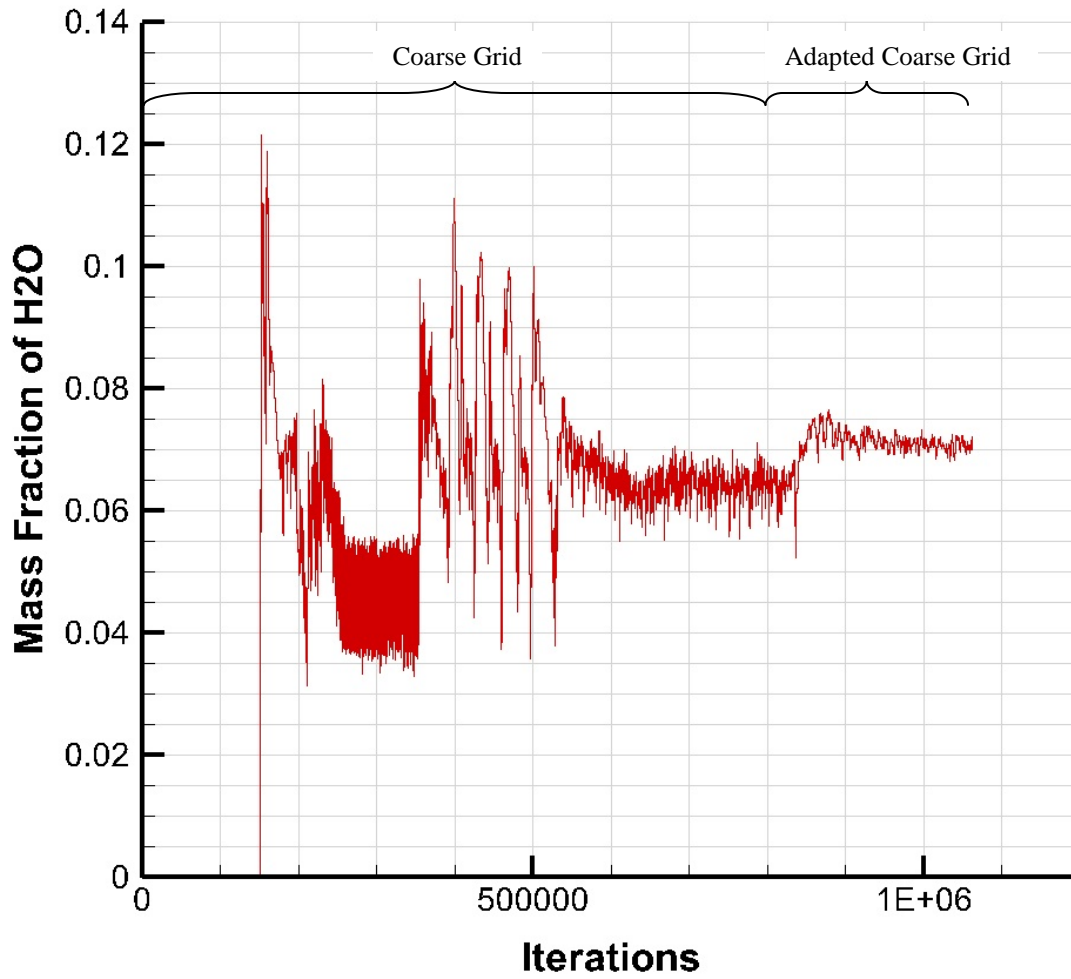


**Figure 29, Convergence History of Water Vapor at Exit Plane, Coarse Grid Adapted with Static Pressure Gradient,  $\Phi = 0.27$**

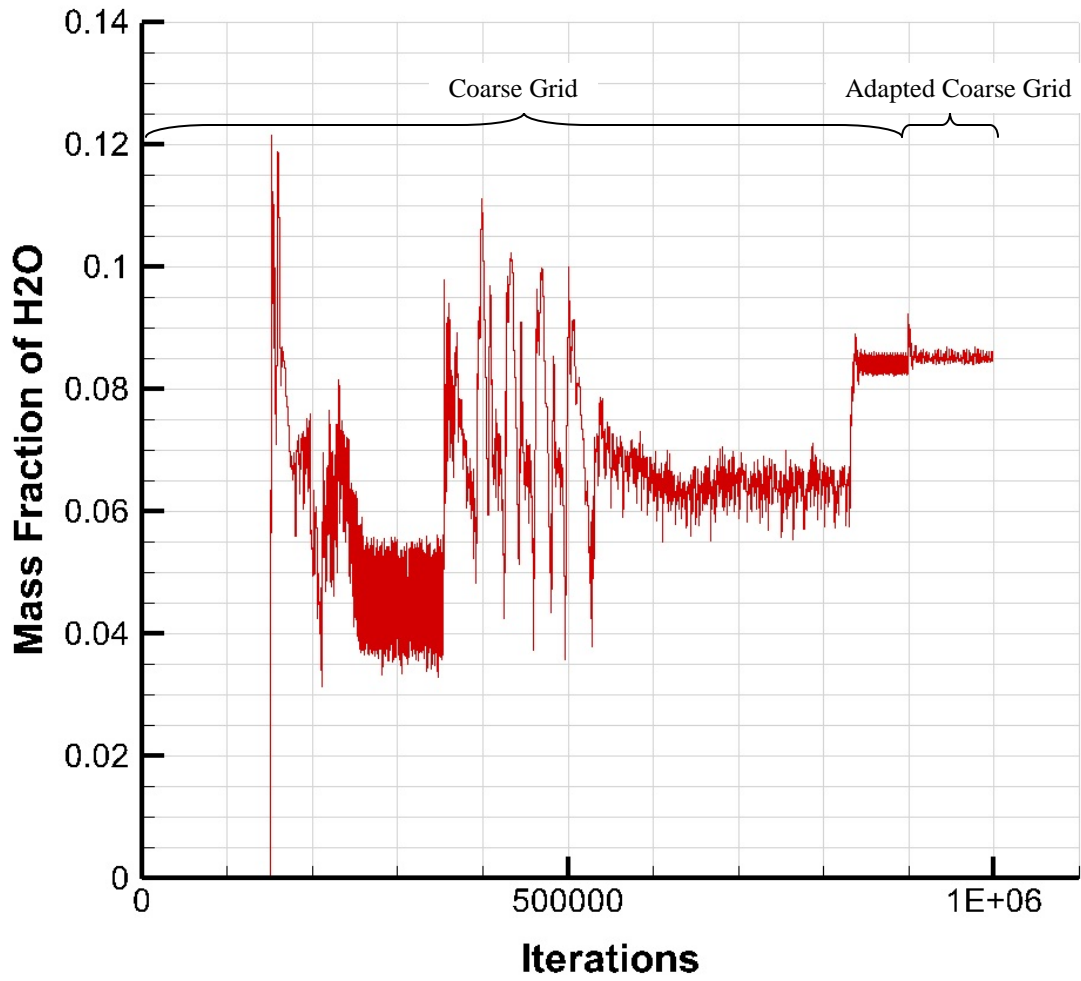


**Figure 30, Convergence History of Water Vapor at Exit Plane, Coarse Grid Adapted with Static Pressure Gradient,  $\Phi = 0.38$**

## VI. Summary and Conclusions

The UVa. direct connect SCF flowpath was modified to a two dimensional version and simulated using the commercial CFD solver ANSYS Fluent. Fuel-off and fuel-on reacting cases at equivalence ratios of 0.27 and 0.38 were run using coarse, medium and fine computational grids. Grid independence was not achieved. The fine grid yields significantly different solutions compared to the coarse and medium grid. The fine grid simulation for  $\Phi = 0.38$  was re-ignited numerically and also run with time-accurate analysis to investigate the cause of discrepancy in solution. However, both attempts gave the same solution as before. With limited computational resources, it is speculated that the fine grid better resolved the boundary layer profile along the walls of the flowpath. This, together with well resolved shocks, could have captured the shock-boundary layer effect and flow separation in better accuracy. As a result, the flow field could be significantly different, as in the fine grid solution. It should be noted that a large number of cells was needed for the two-dimensional model in order for the significant difference in solution to be observed. Future studies may involve using a three-dimensional model of the flowpath to investigate the inconsistency in grid convergence.

The coarse grid was adapted with a matrix of various methods and parameters to emulate the medium and fine grid results. It was found that adaptation based on static pressure gradient provides better improvement in solution compared to other methods and parameters. Increase in combustion efficiency and static pressure distribution which matches the medium grid solution was noted for the case of  $\Phi = 0.27$ . As for  $\Phi = 0.38$ , improvement was not as prominent. Slight increase in combustion efficiency was observed. The static pressure distribution in the combustor better matches the medium grid solution although still being under predicted. It was found that local adaptation with minimal amount of cells could drive the solution towards that of a globally

refined grid. However, the direction at which the solution is being driven by local adaptation may not necessarily be that of the correct or grid independent solution, as shown by the results of this research.

This study demonstrated the effectiveness of grid adaptation in emulating solutions of a more globally refined grid. A coarse grid was able to generate solutions close to that of the medium grid by local adaptation which adds just 25 percent more cells. However, further investigation on grid independence needs to be performed to validate the results. Experimental results and three dimensional simulations of the flowpath will also be needed to conclusively verify the feasibility of using coarse grid plus grid adaptation approach to obtain reasonable solutions with reduced computational efforts for high-speed reacting flows.

## References

1. Dannenhoffer, J.F.III, Baron, J.R., Grid Adaptation for the 2-D Euler Equations, *AIAA 23rd Aerospace Sciences Meeting*, Reno, Nevada, January 14-17, 1985.
2. Hsu, A.T., The Effect of Adaptive Grid on Hypersonic Nozzle Flow Calculations, *AIAA 27<sup>th</sup> Aerospace Sciences Meeting*, Reno, Nevada, January 9-12 1989.
3. Ramakrishnan, R., Singh, D.J., Modeling Scramjet Combustor Flowfields with a Grid Adaptation Scheme, *AIAA Journal*, Vol. 32, No. 5, May 1994.
4. Frauholz, S., Behr, M., Reinartz, B.U., Muller, S., Numerical Simulation of Hypersonic Air Intake Flow in Scramjet Propulsion Using a Mesh-Adaptive Approach, *AIAA Paper 2012-5976*. September 2012.
5. Bhagwandin, V.A., Engblom, W.A., Georgiadis, N.J., Numerical Simulation of a Hydrogen-Fueled Dual-Mode Scramjet Engine Using Wind-US, *AIAA Paper 2009-5382*, August 2009.
6. Vyas, M.A., Engblom, W.A., Georgiadis, N.J., Trefny, C.J., Bhagwandin, V.A., Numerical Simulation of Vitiating Effects on a Hydrogen-Fuelled Scramjet, *AIAA Paper 2010-1127*, January 2010.
7. Engblom, W.A., Bellamkonda, G., Osborne, J.W., Experimental and Numerical Evaluation of Hydrogen Fuelled Dual Mode Scramjet Engine, *AIAA Paper 2012-3291*, June 2012.
8. Rockwell, R.D., Goyne, C.P., Haw, W., Krauss, R.H., McDaniel, J.C., Trefny, C.J., Experimental Study of Test-Medium Vitiating Effects on Dual-Mode Scramjet Performance, *Journal of Propulsion and Power*, Vol. 27, No. 5, September-October 2011.



9. Anderson, J.D., "Quasi-One-Dimensional Flow", Modern Compressible Flow with Historical Perspective, 3<sup>rd</sup> ed, McGraw-Hill, New York, 2004, pp. 218-225.
10. Ansys Inc. 4.4.3 Realizable k- $\epsilon$  Model, Ansys Fluent Index, <http://www.sharcnet.ca/Software/Fluent12/html/th/node60.htm#13904>, Cited June 10 2013.
11. Magnussen, B.F., On the Structure of Turbulence and a Generalized Eddy Dissipation Concept for Chemical Reaction in Turbulent Flow, *19th AIAA Aerospace Science Meeting*, St.Louis, Missouri, January 12-15 1981.
12. Poinso, T., Veynante, D., "Turbulent Non-Premixed Flames", Theoretical and Numerical Combustion, 2<sup>nd</sup> ed, R.T. Edwards, Inc., Philadelphia, PA, 2005, pp. 320-321.
13. Marinov, N.M., Westbrook, C.K., Pitz, W.J., Detailed and Global Chemical Kinetics Model for Hydrogen, 8<sup>th</sup> International Symposium on Transport Properties, October 1995.
14. Warren, G.P., Anderson, W.K., Thomas, J.L., Krist, S.L., Grid Convergence for Adaptive Methods, AIAA Paper 91-1592-CP.